

A Quasar-Anchored Protocluster at $z = 6.6$ in the ASPIRE Survey: I. Properties of [OIII] Emitters in a 10 Mpc Overdensity Structure

JACLYN B. CHAMPAGNE,¹ FEIGE WANG,^{1,2} HAOWEN ZHANG (张昊文),¹ JINYI YANG,^{1,2}
XIAOHUI FAN,¹ JOSEPH F. HENNAWI,³ FENGWU SUN,¹ EDUARDO BAÑADOS,⁴ SARAH E. I. BOSMAN,^{5,6}
TIAGO COSTA,⁷ ANNA-CHRISTINA EILERS,^{8,9} RYAN ENDSLEY,¹⁰ XIANGYU JIN,¹ HYUNSUNG D. JUN,¹¹
MINGYU LI,¹² XIAOJING LIN,¹ WEIZHE LIU,¹ FEDERICA LOIACONO,¹³ ALESSANDRO LUPI,^{14,15,16}
CHIARA MAZZUCHELLI,¹⁷ MARIA PUDOKA,¹ KLAUDIA PROTUŠOVÀ,^{5,6} SOFÍA ROJAS-RUIZ,¹⁸
WEI LEONG TEE,¹ MAXIME TREBITSCH,¹⁹ BRAM P. VENEMANS,²⁰ MING-YANG ZHUANG (庄明阳),²¹
AND SIWEI ZOU²²

(Received –; Revised –; Accepted –)

Submitted to ApJ

ABSTRACT

ASPIRE (A SPectroscopic survey of bIased halos in the Reionization Era) is a quasar legacy survey primarily using *JWST* to target a sample of 25 $z > 6$ quasars with NIRCcam slitless spectroscopy and imaging. The first study in this series found evidence of a strong overdensity of galaxies around J0305–3150, a luminous quasar at $z = 6.61$, within a single NIRCcam pointing obtained in *JWST* Cycle 1. Here, we present the first results of a *JWST* Cycle 2 mosaic that covers 35 arcmin² with NIRCcam imaging/WFSS of the same field to investigate the spatial extent of the putative protocluster. The F356W grism data targets [OIII]+H β at $5.3 < z < 7$ and reveals a population of 124 line emitters down to a flux limit of 1.2×10^{-18} erg s⁻¹ cm⁻². Fifty-three of these galaxies lie at $6.5 < z < 6.8$ spanning 10 cMpc on the sky, corresponding to an overdensity within a 2500 cMpc³ volume of 12.5 ± 2.6 , anchored by the quasar. Comparing to the [OIII] luminosity function from the Emission line galaxies and Intergalactic Gas in the Epoch of Reionization (EIGER) project, we find a dearth of faint [OIII] emitters at $\log(L/\text{erg s}^{-1}) < 42.3$, which we suggest is consistent with either bursty star formation causing galaxies to scatter around the grism detection limit or modest suppression from quasar feedback. While we find a strong filamentary overdensity of [OIII] emitters consistent with a protocluster, we suggest that we could be insensitive to a population of older, more massive Lyman-break galaxies with weak nebular emission on scales > 10 cMpc.

Keywords: galaxies, quasars

1. INTRODUCTION

Dedicated surveys have now revealed a population of > 200 rare, extremely bright quasars at

Corresponding author: Jaclyn B. Champagne
jbchampagne@arizona.edu

$z > 6$, many with measured black hole masses in excess of $10^9 M_\odot$ (e.g., Bañados et al. 2016; Yang et al. 2019; Wang et al. 2021; Fan et al. 2023; Mazzucchelli et al. 2023; Bañados et al. 2023). The existence of these billion-solar-mass black holes < 1 Gyr after the Big Bang poses a major challenge to our understanding of supermassive black hole formation (see review in Volonteri et al. 2021). These bright $z > 6$ quasars are broadly predicted by various simulations to reside in massive host galaxies within the rarest, most massive dark matter halos in the early Universe ($M_h \sim 10^{12.5-13} M_\odot$; Costa et al. 2014; Angulo et al. 2012; Di Matteo et al. 2017; Lupi et al. 2024). This is observationally corroborated by their strong clustering (García-Vergara et al. 2017; Arita et al. 2023).

Given their expected halo masses, the earliest quasars should trace very strong matter overdensities associated with the seeds of present-day galaxy clusters (though the variance on scales larger than a few cMpc is significant, e.g., Angulo et al. 2012). Prior to *JWST*, much effort was invested towards quantifying galaxy overdensities around $z > 6$ quasars based on imaging using either *HST* or large ground-based telescopes. But while overdensities were occasionally found in observations, they certainly were not ubiquitous (e.g., Kim et al. 2009; Bañados et al. 2013; Mazzucchelli et al. 2017b; Ota et al. 2018; Champagne et al. 2023; Rojas-Ruiz et al. 2024). Interpreting these results was extremely challenging given heterogeneous selection techniques, restricted fields of view, and different cosmic volumes probed by various galaxy tracers (e.g., Lyman-break galaxies, Ly α emitters, and dusty star-forming galaxies). Moreover, the limited near-IR sensitivity and poor photometric redshift precision ($\Delta z \gtrsim 1$) afforded by ground and *HST* surveys likely caused all but the strongest true galaxy overdensities around $z > 6$ quasars to be missed. This was also coupled with the uncertainty of the underlying

spatial distribution of companion halos, compounding the issue of observational geometry (e.g. Zana et al. 2023).

Thus, the question of whether the earliest quasars routinely trace strong galaxy overdensities could not be answered without near-IR spectroscopy in wide fields of view (e.g., Lupi et al. 2022). Dark matter simulations predict that galaxy protoclusters are extended beyond tens of comoving Mpc at $z > 6$ (Chiang et al. 2017; Muldrew et al. 2015; Overzier 2016), which cannot be probed with, for example, single ALMA pointings (Champagne et al. 2018). Now, with the power of *JWST*/NIRCam’s wide-field slitless spectroscopy (WFSS) in fields of view on the scale of tens of square arcminutes, we can perform detailed case studies around individual quasar environments.

To this end, two major Cycle 1 surveys emerged targeting the environments of reionization-era quasars. The Emission-line galaxies and Intergalactic Gas in the Epoch of Reionization (EIGER) project (Kashino et al. 2023; Matthee et al. 2023; Eilers et al. 2024) has already begun to use NIRCam’s WFSS mode to characterize the environments and statistical clustering of a sample of six $z \sim 6$ quasars, finding a diversity of overdensity signals. The second, the focus of this paper, is A SPectroscopic survey of bIased halos in the Reionization Era (ASPIRE) project (Wang et al. 2023; Yang et al. 2023). Both of these studies perform grism spectroscopy in F356W with direct imaging in F356W, F200W, and F115W.

In total, ASPIRE targeted 25 $z > 6.5$ quasars in *JWST* Cycle 1 with single NIRCam pointings. This paper focuses on a single quasar field from the ASPIRE sample, which is well-studied at multiple wavelengths. J0305–3150 was originally identified in the VIKING Survey (Venemans et al. 2013, 2016) and lies at $z = 6.61$, containing a $\sim 10^9 M_\odot$ SMBH (Mazzucchelli et al. 2017a). Ota et al. (2018) found

the first hints of an overdensity in this field, using Subaru broad- and narrowband imaging to identify 53 LBGs and 14 LAEs, corresponding to a 3σ and 1σ overdensity respectively across a $30'$ by $30'$ field. Later, Champagne et al. (2023) found an overdensity of LBGs in the field, with $\delta_{\text{gal}} \equiv N_{\text{obs}}/N_{\text{exp}} - 1 = 8.8 \pm 1.8$ based on photometric redshift fitting of 42 galaxies identified with *HST* broadband imaging within a 6.25 arcmin^2 field of view (FOV). Using ASPIRE Cycle 1 data, Wang et al. (2023) identified 41 galaxies at $5.4 < z < 6.9$ in a single NIRCcam pointing (11 arcmin^2) of the same field via the detection of [OIII]+H β , 21 of which were within $\Delta z \pm 0.2$ ($\sim 7800 \text{ km s}^{-1}$) from the quasar. Of those twenty-one, 13 [OIII] emitters were matched to 10 spatially-unresolved LBGs from Champagne et al. (2023). Wang et al. (2023) thus provided evidence for a spectroscopic overdensity extending several comoving Mpc on the sky, which motivated us to target this field again in Cycle 2 with a NIRCcam mosaic covering $6\times$ the area to investigate the extended protocluster structure.

With spectroscopic data in hand and a suite of imaging from prior studies (Ota et al. 2018; Champagne et al. 2023) and NIRCcam (Wang et al. 2023), we can investigate in detail the rest-optical properties of these galaxies and compare them to the general field population towards the end of the epoch of reionization. In this paper (Paper I), we present the galaxies detected in a NIRCcam mosaic of the field of J0305–3150 and evaluate the protocluster nature of the overdensity. The following paper (Paper II; Champagne et al. 2024) presents detailed SED fitting of the galaxies using the full suite of imaging and discusses the environmental dependence of galaxy evolution within the protocluster. We describe our dataset and reduction process with details on our catalog construction for [OIII] emitters and LBGs in §2 and §3. §4 shows the 3D distribution of the filaments in the protocluster.

§5 presents the [OIII] luminosity function and equivalent width distribution for the spectroscopically confirmed protocluster members. In §6.1 we present our interpretation of the environment of the quasar within the protocluster, while we compare to simulations in §6.2 and conclude in §7. Throughout this paper we assume AB magnitudes and a flat Λ CDM cosmology with $H_0 = 70 \text{ km s}^{-1} \text{ Mpc}^{-1}$, $\Omega_\Lambda = 0.7$, and $\Omega_M = 0.3$.

2. OBSERVATIONS AND DATA REDUCTION

2.1. *JWST* Data

J0305–3150 was observed as part of the Cycle 1 *JWST* ASPIRE (A SPectroscopic survey of biased halos In the Reionization Era) program (GO #2078, PI: F. Wang) which targets 25 $z > 6.5$ quasars with F356W grism spectroscopy and F115W/F200W/F356W broadband imaging with NIRCcam. More details about the ASPIRE survey can be found in Wang et al. (2023). Follow-up mosaic observations were performed in Cycle 2 (GO #3325, PI: F. Wang). We use the ASPIRE grism spectroscopy to identify [OIII] λ 5007 emitters, which are complemented by the additional 5-pointing mosaic in Cycle 2 centered on the quasar, for a total area coverage of 35.05 arcmin^2 . We briefly summarize the data reduction and processing to homogenize the data here.

2.1.1. *NIRCcam* WFSS

ASPIRE uses Grism-R with F356W in the long wavelength (LW) channel ($R \sim 1300 - 1600$), with simultaneous observations with F200W in the short wavelength channel (SW). Thus, the quasars are observed with slitless spectroscopy at $3-4 \mu\text{m}$ with deep ($\sim 28 \text{ mag}$ at 5σ) imaging at $2 \mu\text{m}$. The main observations are performed with a 3-point INTRAMODULEX primary dither pattern and each primary position includes two sub-pixel dithers, yielding a survey area of $\sim 11 \text{ arcmin}^2$ per pointing for imaging

+ slitless spectroscopy (the mosaicked area is 35 arcmin^2 accounting for overlaps). We use the SHALLOW4 readout pattern with nine groups and one integration which gives a total on-source exposure time of 4257 s per pointing, with the deepest data centered on the quasar. Full details of the reduction steps including astrometric and spectral calibrations, dispersion modeling, and extraction of spectra can be found in Wang et al. (2023). That study noted a half-pixel offset between the spectral tracing model and the data along the spatial direction, but that the offset along the dispersion direction requires in-flight wavelength calibration that is still not available. They quote a conservative constant offset of $<100 \text{ km s}^{-1}$ which translates to $\Delta z < 0.003$ for the [OIII] emitters, which we adopted here as well.

2.1.2. NIRC*Cam* imaging

To maximize the sky area coverage, both NIRC*Cam* modules are used by ASPIRE for direct imaging. In order to match spectra to their sources from the grism spectroscopy, direct (near the quasar) and out-of-field imaging (to capture sources outside of the NIRC*Cam* field of view whose spectra may land on the WFSS detector) were performed with the same readout pattern as the main observations, with the F115W filter in the SW and the F356W filter in the LW. Therefore, J0305 was observed with F115W, F200W, and F356W, with the latter being the deepest. Reduction of the NIRC*Cam* images was performed using version 1.10.2 of the JWST Calibration Pipeline (CALWEBB). We use the reference files (`jawst_1015.pmap`) from version 11.16.21 of the standard Calibration Reference Data System (CRDS) to calibrate our data. The details of the Stages 2 and 3 steps, including creating background images, the measurement of the $1/f$ noise, astrometric alignment, image drizzling and final background subtraction can be found in Wang et al. (2023); Yang et al. (2023). During the resampling step,

we used a fixed pixel scale of $0.031''$ for the SW images and $0.0315''$ for the LW images with adopted `pixfrac=0.8`. The mosaicked images are further aligned to the reference catalog from *Gaia* DR3 (Gaia Collaboration 2020) for absolute astrometric calibration, yielding precise relative alignment (RMS $\sim 15 \text{ mas}$) and absolute astrometric calibration (RMS $\sim 50 \text{ mas}$). The 5σ depths, calculated by placing random empty $0''.32$ -diameter apertures across the image, are 27.2, 28.0, and 28.3 in F115W, F200W, and F356W respectively.

3. CATALOG CONSTRUCTION

3.1. The [OIII] catalog

We used `SourcExtractor++` (Bertin et al. 2020) on the NIRC*Cam* imaging to create an initial photometric catalog. Details of the `SourcExtractor++` and photometric measurements can be found in Paper II; we use this catalog only as positional priors to extract [OIII] line emitter candidates. We cross-matched our photometric catalog with the catalog of [OIII] emitters reported by Wang et al. (2023), which was extracted only from the central pointing of our mosaic data, using a search radius of $0''.1$ (chosen to be close to the PSF size and to accommodate potential astrometric offsets from the Cycle 1 dataset). Wang et al. (2023) reported 41 [OIII] emitters at $5.3 < z < 6.9$, all of which remain robust and with no positional offsets after using improved reduction procedures.

For the ASPIRE dataset, we (Wang et al. 2023, Wang et al, in prep.) developed a semi-automatic emission line candidate searching algorithm based the continuum-subtracted 2D and 1D spectra. Briefly, for every source identified in the F356W image, we extract a grism spectrum using optimal extraction, which fits and weights a radial profile to the source, without concerns of flux loss as from a boxcar extraction. We produce a median-filtered continuum model with a window size of 51 pixels, which

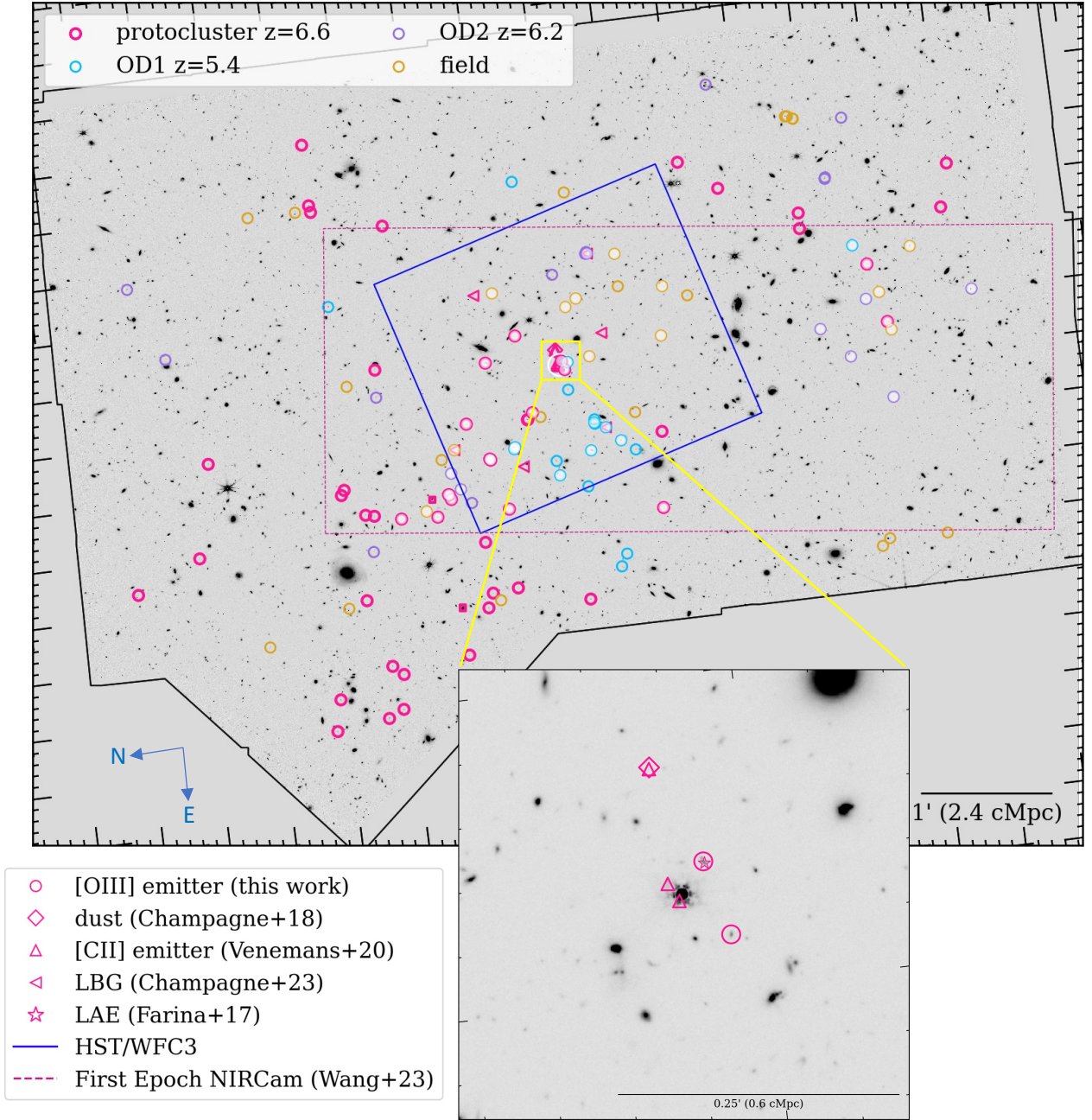


Figure 1. Full F356W six-pointing mosaic surrounding J0305–3150, with the field of view outlined in black. The quasar is depicted at the center with a white circle. The quasar-anchored overdensity members are shown in pink, the overdensities at $z = 5.4$ and $z = 6.2$ are in blue and purple, and the field galaxies at $5.3 < z < 6.5$ are shown in yellow. The blue box shows the WFC3 footprint where galaxies have photometric coverage from *HST*, and the dashed plum line shows the single NIRCcam pointing from Wang et al. (2023) with the quasar centered in Module A. The configuration of the pointings is such that we have the greatest depth in the immediate surroundings of the quasar, so we are most sensitive to faint galaxies in the central regions. The filled points indicate sources already identified in the Cycle 1 data (Wang et al. 2023). Inset: Zoom-in to the central $30''$ surrounding the quasar. Three companion [CII] emitters (Venemans et al. 2020), 1 dust continuum emitter (Champagne et al. 2018), 1 LAE (Farina et al. 2017), and 2 [OIII] emitters (this work; one of them is the LAE) are visible within a few hundred ckpc from the quasar.

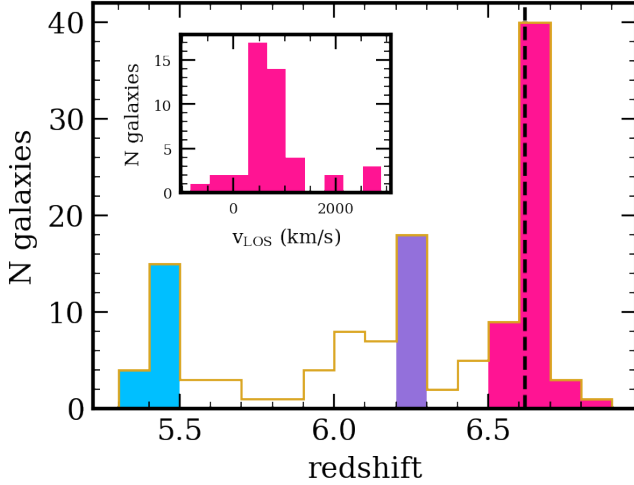


Figure 2. Redshift histogram of all 124 [OIII] emitters identified here, with the three primary overdensities highlighted. The quasar is at $z = 6.614$ (dashed line; Venemans et al. 2019). The inset shows the velocity distribution of galaxies with respect to the quasar, i.e. the galaxies hereafter considered to be members of the quasar-anchored protocluster.

gets subtracted from the extracted spectrum. In a S/N spectrum smoothed to filter out hot pixels and artifacts, we search for $S/N > 1.2$ peaks. To determine if a source is an [OIII] emitter candidate at $z \sim 5 - 7$, we first assume any identified lines with $S/N > 5$ are from [OIII] $\lambda 5008$ and then search for a corresponding [OIII] $\lambda 4960$ and/or $H\beta$ line detected with $SNR > 2$. Sources with three securely identified lines are retained as high-quality candidates, though about 50% of our sources have upper limits ($S/N < 4$) on $H\beta$ fluxes. An example spectrum is displayed in Appendix A.

Combining with the new 5-pointing mosaic across 35 arcmin^2 , our updated line-search procedure yielded 83 new [OIII] emitters which are added to our sample. This corresponds to a total of 53 [OIII] emitters that are members of the overdensity at $z \geq 6.5$ and 71 at $z < 6.5$ (124 in all). The 5σ limiting flux in the deepest central part of the mosaic, assuming a linewidth of 50 \AA ($2\times$ the spectral resolution, approxi-

mately 250 km s^{-1}), is $1.2 \times 10^{-18} \text{ erg s}^{-1} \text{ cm}^{-2}$. This corresponds to a luminosity of $6 \times 10^{41} \text{ erg s}^{-1}$ at $z = 6.6$. There are two serendipitously discovered overdensities along the line of sight at $z = 5.4$ and $z = 6.2$ which we will discuss in detail in §5.

Rest-frame equivalent widths (EW) are measured for the [OIII] emitters using the [OIII] line fluxes (obtained by integrating the best-fit Gaussian to the [OIII] doublet in the 1D spectrum) and the F356W broadband photometry after subtracting out the line contribution, assuming a flat continuum in f_ν .

3.2. The LBG catalog

We use the catalog from Champagne et al. (2023) who identified LBGs using a single pointing of 5-band *HST* WFC3 and ACS imaging. We do not identify any new LBGs within the *HST* footprint that are not already in the [OIII] catalog, nor do we add any new *HST* data covering the WFSS mosaic. Champagne et al. (2023) searched for LBGs in a wide redshift range of $\Delta z = 1.5$ due to the coarse sampling of the SED with only *HST*. We cross-matched that LBG catalog with our new photometric catalog which used F356W as the detection image (see Paper II) and included the NIRCcam photometry to refit their SEDs using EAZY (Brammer et al. 2008). Of the 42 $z = 5.9 - 7.6$ LBGs reported in Champagne et al. (2023), three are not detected in the F356W catalog, but they were classified as “marginal” in the original work, corresponding to low-SNR ($< 4.5\sigma$) detections in F160W and $< 80\%$ of the photometric redshift PDF lying at $z > 6$; therefore, we discard them as likely not to be high-redshift galaxy candidates given the deeper imaging with NIRCcam. Cutouts of these discarded LBGs are shown in Appendix B. Of the remaining 39 LBGs, 18 do not have photo- z ’s consistent with $z_{\text{qso}} \pm 0.3$ after the inclusion of NIRCcam and Subaru photometry (this is the median offset between $z_{[\text{OIII}]}$ and z_{phot} ; see paper II for template SED fit-

ting), 11 are confirmed [OIII] emitters not at the quasar redshift ($5.4 < z < 6.3$), and 3 [OIII] emitters are already included in our primary overdensity sample. The remaining 7 are still robust LBGs with $z_{\text{phot}} \geq 6.31$.

Since the grism data is sensitive to a wide range of $5.3 < z < 7$, any LBGs from Champagne et al. (2023) should have been detected in [OIII] even for those with high photo- z uncertainty. While they might be lower- z interlopers given the sparse rest-UV/optical filter coverage, the total lack of emission lines in the remaining LBGs could be due to an inherent faintness of nebular emission, which could be caused by rapid bursts and lulls in the star formation history occurring on < 10 Myr timescales (e.g., Endsley et al. 2024a; Faisst & Morishita 2024; Trussler et al. 2025). We hypothesize that they have lower specific star formation rates which would result in undetectable [OIII] emission at the ASPIRE flux limit, a consequence of stochastic star formation histories (discussed further in Paper II). For those LBGs which are not confirmed in [OIII] but have robust photo- z estimates (defined as $> 80\%$ of the EAzY redshift PDF lying between $6.4 < z < 6.8$), we derive an upper limit on the EW using the observed F356W magnitude and a 5σ limiting line flux at the location of the LBGs ($\approx 2 \times 10^{-18} \text{ erg s}^{-1} \text{ cm}^{-2}$).

4. A PROTOCLUSTER AT $Z = 6.61$

The quasar overdensity consists of 53 galaxies at $6.5 < z < 6.8$ ($\Delta V \approx 10,000 \text{ km s}^{-1}$)¹, with a maximum extent of $417''$ or 17 proper Mpc. Within the overdensity, a surprising 41 lie at exactly the quasar redshift ($\Delta V < 1000 \text{ km s}^{-1}$).

¹This is quite a bit larger than the typical protocluster definition used in the literature of $1000\text{--}2000 \text{ km s}^{-1}$ along the line of sight, but because the overdensity's redshift distribution is a roughly continuous Gaussian (Figure 2), we consider all galaxies in this velocity range to be members for now.

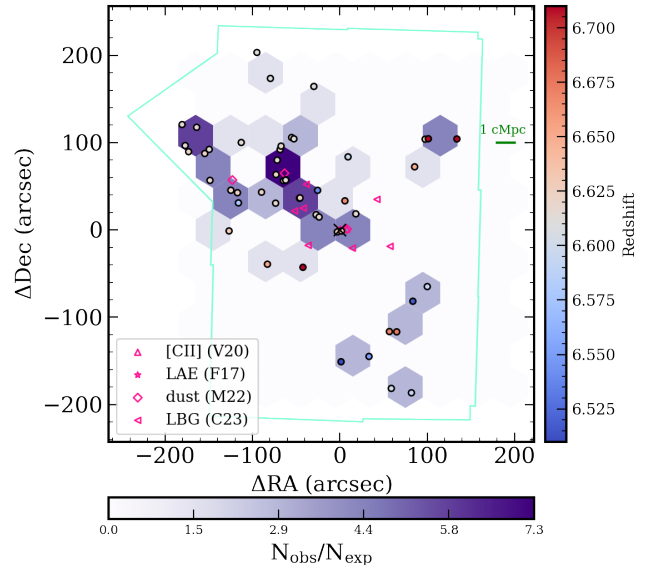


Figure 3. 2D representation of spectroscopically confirmed [OIII] emitters at the quasar redshift (circles). The quasar is marked as the large black \times ; galaxies identified via other tracers are marked in pink symbols. The hexbin histogram (bottom colorbar) denotes the 2D overdensity of [OIII] emitters with respect to the UV luminosity function at $z = 6$ (Finkelstein et al. 2015), showing that the overdensity is stronger in a filament pointing away from the quasar. The right colorbar denotes the redshift of individual galaxies, centered on the quasar redshift. The green outline depicts the footprint of the mosaic.

Two other overdensities are revealed in the full distribution of [OIII] emitters: a compact overdensity at $z = 5.35 - 5.45$ ($\Delta V \approx 4000 \text{ km s}^{-1}$) consisting of 20 galaxies extended across $240''$ (10 pMpc), and a more extended overdensity ($385''$ or 16 pMpc) at $z = 6.2 - 6.3$ ($\Delta V \approx 3000 \text{ km s}^{-1}$) composed of 18 galaxies. The remaining 33 line emitters between $5.5 < z < 6.2$ comprise our field sample. This serendipitous confluence of line-of-sight overdensities helps to explain the high number of LBGs found in this field by Champagne et al. (2023), but the number of galaxies with [OIII]-based spectroscopic confirmation at the quasar redshift remains remarkable.

Figure 1 shows the F356W image with all of the [OIII] emitters overlaid, denoting the quasar overdensity members, the lower redshift overdensities, and the field galaxies, in addition to other galaxies (dust continuum and [CII]) identified in the field by ALMA (Champagne et al. 2018; Venemans et al. 2020; Meyer et al. 2022). The redshift histogram of all 124 line emitters is shown in Figure 2, highlighting the three primary overdensities. The inset shows all galaxies within $\Delta z \pm 0.15$ from the quasar; while these galaxies are likely not *all* associated with the same structure at such a wide line-of-sight distance, the overdensity signal remains strong across a continuous range in redshift at $6.5 < z < 6.8$ and a transverse area of $(10 \text{ cMpc})^2$, so we consider them all to be members for the sake of this study. Basic information about the [OIII] emitters in the protocluster can be found in Table 1.

Figure 3 shows a 2D representation of the overdensity around the quasar, highlighting a filament extending behind the quasar across a transverse distance of $\sim 5 \text{ cMpc}$. The 2D overdensity hexbins are calculated based on the area expected to contain 1 LBG at $M_{UV} < -19$ according to the luminosity function at $z = 6.6$ parameterized by Finkelstein (2016). The quasar actually does not sit at the center of the overdensity, but instead inhabits the SW side of the spatial distribution. Further, it lies at the lower end of the galaxy redshift distribution by about 500 km s^{-1} . The full overdensity extends well into the NIRCcam mosaic, with galaxies at the quasar redshift found within a $(10 \text{ cMpc})^2$ box on the sky. In fact, the overdensity may extend well beyond the current FOV given that many sources are found on the comparatively shallow edges of the mosaic (see exposure map in Figure 4). It is distinctly distributed across multiple overdense filaments, with the densest region found about $1 - 2 \text{ cMpc}$ from the quasar at very slightly lower redshift ($z_{\text{qso}} = 6.614$,

$z_{\text{fil}} = 6.618$). This is comparable to the redshift uncertainty of $\delta z = 0.003$ and could potentially be due to peculiar motion, but regardless the quasar still does not lie at the spatial center of the overdensity. Observationally, protoclusters identified at lower redshift in the fields of DSFGs or AGN are often not centered on the “main” galaxy (e.g., Dannerbauer et al. 2014; Cucciati et al. 2018; Toshikawa et al. 2024) and are observed in an unrelaxed (i.e., non-spherical) distribution. From a theoretical perspective, the BlueTides simulation (Di Matteo et al. 2017) finds that the most massive SMBH are not necessarily in the most spatially overdense regions, but instead in specific environments that favor radial matter inflows (perhaps in this case, on the edge of the overdensity).

Notably, as seen in the inset of Figure 1 and in Figure 3, the immediate environment of the quasar is characterized by a rich population of neighboring galaxies. There are multiple submm-detected galaxies (Venemans et al. 2020) not seen in [OIII], and there is a relative dearth of [OIII] emitters compared to the strong overdensities further from the quasar; we revisit the physics of this in §6.1. This lack of line emitters in the immediate vicinity of the quasar has been seen in other studies tracing LAEs, albeit with much larger “holes” on the scale of 5 pMpc (e.g., Lambert et al. 2024). Given the richness of the overdensity within a relatively small area on the sky — consistent with theoretical expectations (e.g., Overzier et al. 2009) — we strongly suspect that this is a bona fide galaxy protocluster, i.e. a progenitor to a massive cluster of $M_h \sim 10^{14} - 10^{15} M_\odot$ at later times (e.g., Costa et al. 2014).

5. THE [OIII] SAMPLE

5.1. Luminosity function

We next construct the luminosity function (LF) of our [OIII] emitters and compare our findings with the blank field [OIII] LF measured

in the $5.3 < z < 6.9$ in the fore/background of quasars from the EIGER project (Matthee et al. 2023; Kashino et al. 2023). The luminosity function is the usual formula:

$$\phi[\text{Mpc}^{-3}d\log L] = \frac{N}{V_{\text{max}}C} \quad (1)$$

where C is the completeness, N is the number of objects per bin, and V_{max} is the detectable volume subtended by our survey. We bin the [OIII]-emitters in bins of $\log(L/\text{erg s}^{-1}) = 0.2$ and compute V_{max} as a function of redshift and luminosity. Since the sensitivity of NIRCcam WFSS is position- and wavelength-dependent, this translates to a redshift dependence of the detectability of [OIII] in addition to the overall luminosity limit. The survey volume is computed following Sun et al. (2023): for a specific redshift, we compute the effective sky area based on the spectral tracing and grism dispersion models in order to construct RMS maps, done using continuum-subtracted WFSS stage2 cal files. The maximum sky area at each redshift is the area of the RMS map with values smaller than the maximum RMS for a line detection of $\log(L/\text{erg s}^{-1}) = 42$.

To measure completeness, we run 1D source injection simulations. We begin with a noise spectrum with the average line-free rms of our sample at the deepest point of the mosaic (centered on the quasar) which is perturbed within 1σ for every realization. Then we insert Gaussian emission lines with the same wavelength resolution as the real data at a randomly sampled range of intrinsic luminosities ($41 < \log(L/\text{ergs}^{-1}) < 44$), redshifts ($5.3 < z < 7$), and intrinsic FWHM (drawing from a Gaussian centered on 200 km/s with $\sigma = 50$ km/s). We then re-fit the Gaussian to the line and measure the recovered flux and SNR. The completeness varies as a function of wavelength, so we repeat this procedure in bins of $\delta z = 0.1$ such that the completeness is measured as a function of both luminosity and redshift. Figure 4 shows

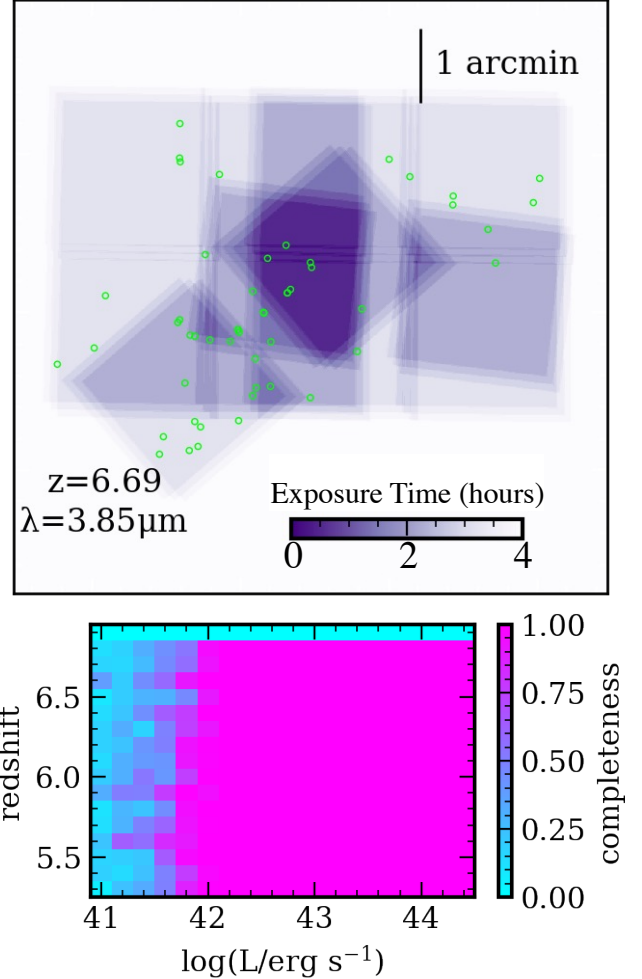


Figure 4. *Top:* Exposure map for the F356W grism mosaic centered at $\lambda_{\text{obs}}=3.85 \mu\text{m}$, or $z = 6.69$. The locations of the protocluster members are denoted with green circles. *Bottom:* Results of our 1D completeness simulations as a function of redshift and input line luminosity, calculated for the deepest central part of the mosaic. The completeness at each location is scaled by the measured RMS of a given line relative to the RMS in the deepest part of the mosaic.

the exposure map for the mosaic as well as the results of our completeness simulations in the deepest part of the mosaic. We find a 100% recovery rate of galaxies at the quasar redshift above $\log(L/\text{erg s}^{-1}) = 42.0$ in the center of the mosaic at $z = 6.69$. For each source at a given location on the exposure map, the value of the completeness moves along the luminosity axis

by the ratio of the RMS at that location relative to that in the deepest exposure².

Figure 5 shows the results of our [OIII] luminosity function for the overdensity samples and the field sample. We calculate the quasar overdensity factor by first integrating the [OIII] luminosity function derived by [Matthee et al. \(2023\)](#) for the EIGER project, who searched for [OIII] emitters with an identical observational setup to ASPIRE in the field of the $z = 6.3$ quasar J0100+2802 in a 26 arcmin² mosaic. We normalize the EIGER LF by the area (35 arcmin²) and volume covered by our field to calculate the expected number of [OIII] emitters between $6.5 < z < 6.8$ and arrive at a lower limit of $\delta_{\text{gal}} \equiv N_{\text{obs}}/N_{\text{exp}} - 1 = 3.7 \pm 1.5$. However, the 53 galaxies in the overdensity are distinctly clustered in a (10 cMpc)² box on the sky (roughly 200×200 arcsec²), so if we instead integrate the EIGER luminosity function in this smaller region to arrive at the expected number of [OIII] emitters, $\delta_{\text{gal}} = 12.5 \pm 2.6$. This is consistent with $\delta_{\text{gal}} = 12$ found by [Wang et al. \(2023\)](#) in a single NIRCcam pointing of the J0305 field. Thus, the filamentary structure extending well into the NIRCcam mosaic footprint remains $> 10\times$ overdense with respect to the field at least out to $R=10$ cMpc (possibly further, given that the structure extends to the edge of the mosaic), consistent with the size of protoclusters at $z > 6$ (e.g., [Chiang et al. 2017](#)).

The luminosity function of the quasar overdensity reveals two curious features: the slope of the protocluster LF at the bright end exhibits a sharper decline than the field relation, and there is a turnover in the protocluster LF at $\log(L/\text{erg s}^{-1}) = 42.4$. By scaling the blank field luminosity function in the foreground of the EIGER quasar J0100+2802 to the area cov-

ered by our survey, we would have expected to find a handful of bright ($\log(L/\text{erg s}^{-1}) > 43$) objects (14 ± 3 in the field at $5.3 < z < 6.5$, 2.2 ± 1 in the quasar overdensity), but this is not reflected either in the field nor the protocluster. A simple Kolmogorov-Smirnov (KS) test between the protocluster [OIII] flux distribution and the field (normalized to the comoving volume of the protocluster within $\Delta z = 0.3$) shows a p -value of 0.35, so the two distributions are not distinguishable. However, we are limited by comparing only two fields that are likely subject to strong field-to-field variance (see, e.g., more results from EIGER; [Eilers et al. 2024](#)). The lack of bright galaxies is not statistically significant, as cosmic variance is particularly dominant at the bright end, contributing an additional 78% to the fractional error on the number counts ([Trenti & Stiavelli 2008](#)).

More interesting than the lack of [OIII]-bright galaxies, however, is the turnover at the faint end. Our 5σ limiting line luminosity at $z = 6.6$ is 6×10^{41} erg/s, and we are presumably complete above 10^{42} erg/s at all redshifts between $5.4 < z < 6.8$ according to our 1D injection simulations. Further, the field is statistically consistent with no turnover, showing agreement with the EIGER field LF within 1σ at $\log(L/\text{erg s}^{-1}) < 42.2$, so we do not believe this is due to completeness. If we normalize the observed protocluster LF to the expected number in the field at $\log(L/\text{erg s}^{-1})=42$, we find that the two faintest bins are discrepant with the field at 3σ significance. Therefore, we explore the possibility that this turnover is due to a physical scenario affecting the observed luminosity distribution rather than a selection effect.

A genuine dearth of faint galaxies compared to bright galaxies within the protocluster could point to physics governing the strength of [OIII] emission, which varies on the timescale of the lifetime of O stars (about 10 Myr; [Eldridge & Stanway 2022](#)). A population of intrinsi-

² Note that NIRCcam Module A is about 20% more sensitive than Module B in the same exposure time, but this is accounted for by using the measured RMS at a given location in the mosaic.

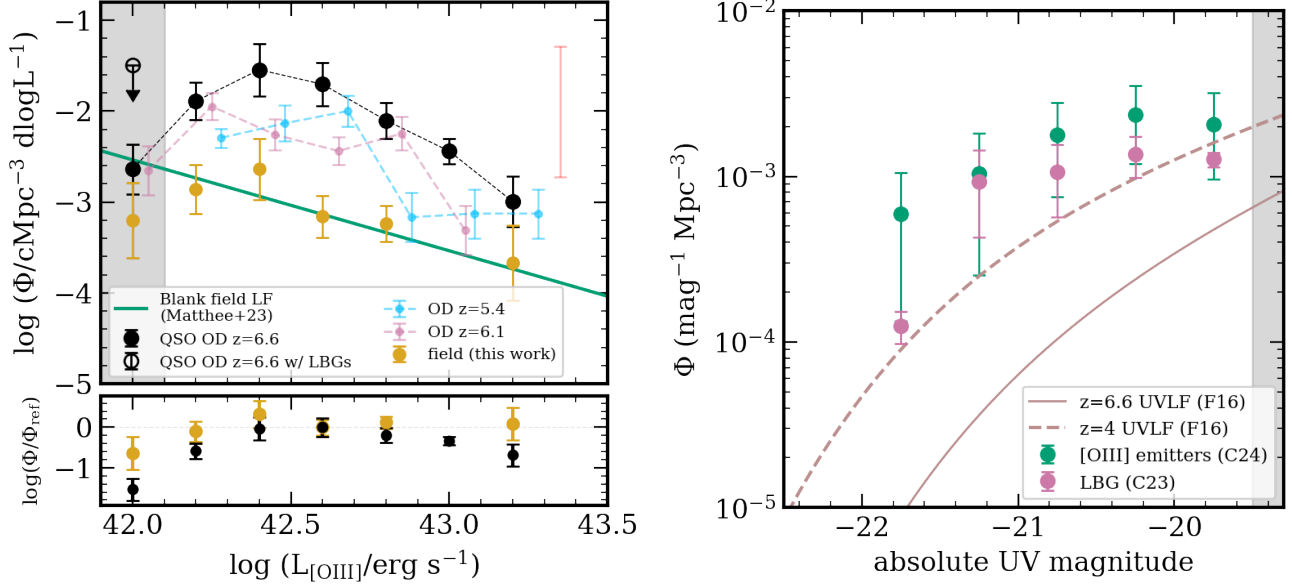


Figure 5. *Left top:* Luminosity function of the [OIII] emitters in our sample. The black points indicate members of the protocluster (empty point indicates the upper limit when including LBGs not detected in [OIII]); the blue and pink points indicate the overdensities at $z < 6.5$. The green line is the blank field luminosity function from EIGER (Matthee et al. 2023), and the filled gold points are the field galaxies in our sample that do not belong to the three overdensities. The grey shaded regions in both panels indicate where we are $< 80\%$ complete, and the red error bar indicates the characteristic error attributed to cosmic variance. The quasar overdensity is an order of magnitude above the blank field expectations but the shape is dissimilar, with a preference for fainter galaxies and a slight dearth of the brightest galaxies. *Left bottom:* The ratio of the field (gold) and protocluster (black) luminosity functions to the EIGER blank field LF, normalized at $\log(L/\text{erg s})=42.6$, showing that the protocluster turnover is significant at $> 3\sigma$ while the field sample is consistent with EIGER within 2σ at any luminosity. *Right:* The UV luminosity function within the quasar protocluster of our [OIII] emitters and LBGs from Champagne et al. (2023). M_{UV} is calculated from the best-fit SEDs presented in Paper II. The redshift-parameterized UVLFs at $z = 6.6$ and $z = 4$ from Finkelstein (2016) are shown: both the [OIII] emitters and the LBGs are consistent with having undergone more rapid evolution than the field by several hundred Myr.

cally faint (i.e. below the grism detection limit) galaxies with respect to their nebular emission could point to the idea that the majority of the galaxies in the protocluster are undergoing less recent star formation. This could be the result of more massive and evolved galaxies having higher metallicity and higher continuum, and thus weaker [OIII]. This is supported by the fact that, if we assume the 7 LBGs are at the quasar redshift and calculate the upper limits of their [OIII] luminosity by using their observed F356W magnitude and assuming the median EW of our sample, they would be below our nominal detection completeness limit

but could contribute to the faintest bin in our LF — effectively, the turnover in the luminosity function disappears (empty circle in the left panel of Figure 5). However, we cannot immediately rule out that quasar feedback could also influence the number counts of faint [OIII] emitters. Yet we also note, qualitatively, that a similar downturn at the faint end of the LF is seen in the two lower-redshift overdensities. This could imply that it is not the mere existence of the quasar influencing the [OIII] distribution (though, normalized to the EIGER LF at $\log(L/\text{erg s}^{-1})=42$ as above, the discrepancy in the lower-redshift overdensities is significant

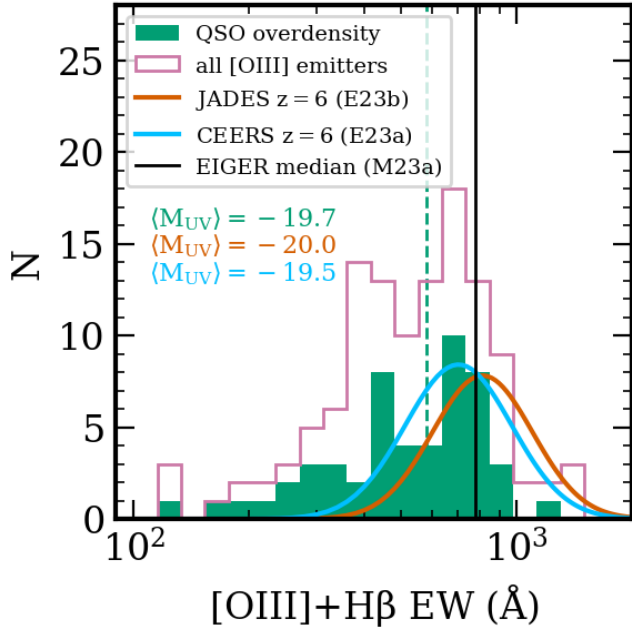


Figure 6. Distribution of $[\text{OIII}]+\text{H}\beta$ equivalent widths in the full sample of 124 emitters (pink) and the protocluster sample (green, with median value shown with a dashed line). We compare to the JADES “bright” sample (orange) from [Endsley et al. \(2023b\)](#) and the CEERS “faint” sample (blue) from [Endsley et al. \(2023b\)](#), with the median M_{UV} of each sample labeled in the corresponding colors. The median EW from EIGER ([Matthee et al. 2023](#)) is shown in black. This sample, despite having similar rest frame UV magnitudes and redshift, trends towards weaker line emission than previous studies of field galaxies.

only at the 2–3 σ level). We return to this point in Section §6.2.

Figure 5 also shows the luminosity function of the two lower-redshift overdensities mentioned in §3.1. These show a similar order of magnitude overdensity above the EIGER relationship and our field LF. It is beyond the scope of this paper to declare whether these are also protocluster structures, but we note it would be interesting to follow them up with further observations. An analysis of the galaxy properties of all three overdensities (quasar and line-of-sight) is left to Paper II.

5.2. $[\text{OIII}]+\text{H}\beta$ strength

Next, in Figure 6 we turn to the nebular line equivalent width distribution, which is a proxy for the ratio of young stellar populations (nebular emission lines powered by OB stars) to older populations (powering the stellar continuum). The median EW of the protocluster population measured from the grism spectra is $580 \pm 15 \text{ \AA}$. The sample of non-overdensity galaxies in the field shows a marginally higher median and spread with $630 \pm 130 \text{ \AA}$; this is more comparable to the median EW of $650_{-90}^{+110} \text{ \AA}$ of UV-bright galaxies in COSMOS ([Endsley et al. 2021](#); [Whitler et al. 2023](#)). On the other hand, [Endsley et al. \(2023a\)](#) finds that the median $[\text{OIII}]+\text{H}\beta$ EW is 780 \AA for UV-faint ($M_{UV} \sim -19.6$) LBGs at $6 < z < 8$ with a dispersion of ~ 0.3 dex; an even higher median of 890 \AA is found for the JADES sample at similar redshift ([Endsley et al. 2023b](#)). However, we note that [Endsley et al. \(2023b\)](#) and [Endsley et al. \(2021\)](#) derive their EW from photometric excesses rather than spectra, which have photometric redshift uncertainties and could induce overestimates of the EW if the continuum or contribution of other faint lines are underestimated. To instead compare with spectroscopic samples, our measured median EW is also below the EIGER median stack value of $845 \pm 70 \text{ \AA}$ ([Matthee et al. 2023](#)), discrepant with our protocluster at 3σ . This could be a systematic effect in our data, but we note that the EIGER median stack excludes galaxies at the redshift of the quasar, so this could potentially suggest a physical difference in the nebular line emission between galaxies within and outside of overdensities — deeper data or observations of more quasar fields would be required to draw more firm conclusions.

Studies differ on the definition of an extreme emission line galaxy (EELG) but here we use the definition of $\text{EW}([\text{OIII}]+\text{H}\beta) > 750 \text{ \AA}$ (e.g., [Boyett et al. 2024](#)). Only 10/53 ($19 \pm 10\%$)

of the protocluster galaxies satisfy this definition while 11/33 ($33 \pm 15\%$) field galaxies can be considered EELGs. Thus, the fraction of EELGs in the protocluster is lower at the 2σ level according to Poisson and small number statistics. It is consistent with the fact that, despite our area coverage which is wide enough to pick up a handful of rare bright objects, we observe the majority of the [OIII] emitters in the protocluster to be rather faint, pointing to an environmental effect. We therefore suggest that the EW distribution in the protocluster could be biased low due to the presence of more evolved galaxies with earlier formation times, resulting in low nebular emission and high continuum from the dominating presence of moderately-aged stars. While we acknowledge that the field ($N = 33$) and protocluster ($N = 53$) samples are consistent with being drawn from the same EW distribution (with a KS p -value of 0.21) and that the EELG fraction is discrepant only at 2σ , the discrepancy between the protocluster and much larger field samples from blank field surveys remains strong at $> 3\sigma$.

Going beyond the spectroscopic data, the question remains, are quasar companion galaxies preferentially brighter compared to the field? We finally compare our results to the UV luminosity function derived in the field (Finkelstein 2016). Champagne et al. (2023) suggested a preferential enhancement of bright ($M_{UV} < -20$) LBGs in the vicinity of $z > 6$ quasars, including J0305–3150, even after correcting the faint end for completeness. Computing the LBG luminosity function in similar bins as the field UV luminosity function of Finkelstein (2016), they found that the slope and normalization of the LBG luminosity function in the field of J0305–3150 was most consistent with the field UVLF at $z = 4$, suggestive of accelerated evolution compared to the field. Now that the [OIII] emitters in the same field are spectroscopically confirmed, we can return

to the question of whether brighter galaxies prevail in the overdensity, or galaxy evolution is enhanced in the full mass range we probe.

While the [OIII] luminosity distribution peaks at relatively low luminosities, we find that the M_{UV} distribution of the [OIII] emitters (measured from their rest-frame SEDs at 1500 \AA , see Paper II for SED details) follows the same slope as that of the LBGs in Champagne et al. (2023): a flattening of the bright end most consistent with evolution accelerated by several hundred Myr (Figure 5, right panel). This is in line with descendant populations, i.e., more evolved bona-fide protoclusters, at $z = 2 - 4$. For example, Hill et al. (2020) and Pensabene et al. (2024) and both find preferential enhancements of bright galaxies within protoclusters at cosmic noon, implying that more massive galaxies evolve faster than their lower-mass counterparts. This is consistent with the distribution of low [OIII]+H β EWs, implying older ages (and thus lower specific star formation rates) and higher metallicity among massive galaxies, as both effects contribute to lowering the H β + [OIII] equivalent width.

6. DISCUSSION

6.1. Immediate Quasar Environment

Figure 1 clearly shows a very busy immediate (~ 100 kpc) environment around the quasar, marked by 3 [CII] emitters (Venemans et al. 2019), a dust continuum emitter (Champagne et al. 2018), one LAE (Farina et al. 2017), and 2 [OIII] emitters from this work (one of which is the LAE)³. Note that the three [CII]-emitters from Venemans et al. (2019) and the dust continuum emitter from Champagne et al. (2018) are each found in single ALMA pointings ($\sim 25''$ diameter in Band 6), but no other [CII] or dust

³ In Paper II, we search for AGN activity in the protocluster members, but for now we assume all of the [OIII] emitters are normal star-forming galaxies.

sources are found in a 1.1' mosaic centered on the quasar (Wang et al., in prep.).

It is interesting to note the relative dearth of [OIII]-emitting galaxies within 100 kpc from the quasar host compared to the much stronger overdensities found further away from the quasar (Figure 3). One way to explain this could be that the quasar host galaxy has grown through major mergers with its immediate neighbors. The [CII] emitters without [OIII] counterparts could imply the existence of massive gas reservoirs but with relatively low instantaneous star formation, which would result in a non-detection of the short-lived [OIII] line. Indeed, Venemans et al. (2019) suggest that the small molecular gas masses ($\sim 5\times$ smaller than the quasar host) and unusual kinematics of the [CII] companion galaxies could imply prior interactions with the host galaxy.

A second explanation for the perceived lack of galaxies very close to the quasar is the result of high dust extinction in the rest-optical. While Wang et al. (in prep.) finds no dust continuum counterparts for the [OIII] emitters nor new sources, the quantity of dust could be below the ALMA detection limit but still significant enough to weaken the [OIII] or indeed the Ly α line. In fact, Ota et al. (2018) imaged this field with on a much wider FOV with Subaru and found 14 narrowband-selected LAE candidates at the quasar redshift, but none closer than 2 arcmin (0.5 cMpc) from the quasar. Galaxies very close to the quasar could thus be undergoing a dustier mode of star formation than those on the outskirts of the overdensity. Venemans et al. (2019) measures SFRs for the [CII] companions in the range of 25–160 $M_{\odot} \text{ yr}^{-1}$ — which, again, have no [OIII] counterparts — so indeed some vigorous star formation is taking place not accounted for by our [OIII] selection method.

A final way to explain the relative dearth of [OIII] emitters very close to the quasar host is through radiative feedback from the quasar.

Indeed, Yang et al. (2023) present blueshifted [OIII] outflows from quasar hosts at similar redshift which could be the result of radiatively driven AGN feedback in kinetic mode, i.e., where radiation pressure produces outward motion of heated gas. Photoionization heating from the central quasar can suppress star formation in surrounding low-mass haloes within the so-called proximity zone, whose size is largely determined by the quasar lifetime and UV luminosity (Satyavolu et al. 2023). The photoionization heating can be described by the quantity J_{21} (Kashikawa et al. 2007; Bosman et al. 2020). This quantity, relating the quasar's UV intensity at the Lyman limit (912 Å) to its environment, is typically applied to the low-mass haloes hosting Lyman- α emitters (LAEs). Assuming that the low-mass [OIII] emitters (median stellar mass $10^8 M_{\odot}$; see SED details in Paper II) occupy similar haloes, we calculate the UV flux density as a function of distance to the quasar using the following equation:

$$F_{\nu}^Q = \frac{L(\nu_L)}{4\pi r^2} \quad (2)$$

where

$$L(\nu_L) = 3631 * 4\pi D_L^2 10^{-0.4m_{1450}} \left(\frac{912}{1450} \right)^{-\beta} \quad (3)$$

where $m_{1450} = 20.89$ mag (Venemans et al. 2013), β is the continuum slope which is measured to be -0.66 using archival photometry of the quasar (Protušová in prep.), r is the angular diameter distance from the quasar, and D_L is the luminosity distance to the quasar. Then J_{21} is the isotropic UV intensity $J/10^{-21} \text{ erg s}^{-1} \text{ cm}^{-2} \text{ Hz}^{-1} \text{ sr}^{-1}$ where $J = F_{\nu}^Q/4\pi$. Evaluating these equations at 2 pMpc (15.2 cMpc, approximately the full angular extent of the protocluster) we find that $F_{\nu}^Q = 1.1 \times 10^{-19} \text{ erg s}^{-1} \text{ cm}^{-2} \text{ Hz}^{-1}$, and thus $J_{21} = 9.8 \pm 0.9$.

Some studies (e.g., Kashikawa et al. 2007; Chen 2020) have suggested that values of $J_{21} >$

1 can completely suppress star formation in low-mass halos, but we do not see such an effect in our field as there are indeed at least 56 galaxies within 2 pMpc of the quasar. For one, we expect that the [OIII] emitters occupy halos of $\sim 10^{10} M_{\odot}$ (see §6.2) which is above the halo mass limit where we expect to see significant suppression (e.g., [Bosman et al. 2020](#)). Secondly, not all galaxies in the vicinity of the quasar will be equally exposed to the quasar radiation due to 1) patchy dust obscuration within the host galaxy and 2) the fact that the UV flux from the quasar is radiated in a beam with a modest opening angle rather than isotropically. Such a double-cone shape is indeed accommodated by the non-spherical distribution of [OIII] emitters (Figure 3), though we note the mosaic is not uniformly sensitive across the whole area. Modest suppression of slightly higher-mass halos may still be occurring in the very inner regions close to the quasar, where $J_{21} > 100$, given the low number of close companions. This is supported by the shape of the [OIII] luminosity function (Figure 5), where we see potential hints of suppression of [OIII] emitters at the faint end (i.e., where the LF is the steepest.) We explore in the next section whether the turnover in the LF could primarily be attributed to intrinsic star formation properties of the galaxies or a direct result of interaction with the quasar.

6.2. Comparison to simulations

Given the extended filamentary nature of the quasar protocluster spanning over 12 cMpc on the sky and $\Delta z = 0.2$ along the line of sight, we can already conclude the structure is not virialized. Simulations suggest that galaxies in the crowded cores of protoclusters will merge to become the brightest cluster galaxy (BCG) at early times ($z > 3$; [Rennehan et al. 2020](#)), but the spatially-wide, non-spherical distribution of galaxies in this reionization-era protocluster does not imply that it is currently approaching any relaxed state. Therefore, we can-

not use the virial theorem to estimate a total halo mass for this structure, nor can we comment on whether this structure will ever fully collapse into a galaxy cluster. Bearing this in mind, we can still evaluate the protocluster in the context of very large halos in the early Universe by considering halos with similar masses to that of the quasar host galaxy. We finally wish to investigate whether the observed population of [OIII]-emitters follows what we would expect from simulations of such massive halos.

Cosmological hydrodynamical simulations such as BLUETIDES ([Di Matteo et al. 2017](#)) as well as empirical models such as TRINITY ([Zhang et al. 2024](#)) suggest that quasars hosting SMBH masses similar to J0305–3150 should occupy massive halos on the order of $M_h \sim 10^{12} M_{\odot}$. We first compare with halos and galaxies in the UNIVERSEMACHINE mock catalogs based on the *Small MultiDark-Planck* N-body simulation (SMDPL, box size: 400 Mpc/h, particle number: 3840^3 , halo mass limit: $\sim 10^{10} M_{\odot}$ ⁴; see [Klypin et al. 2016](#)) as well as the quasar host halos based on the cosmological zoom-ins from [Costa \(2024\)](#).

6.2.1. UniverseMachine

We use the UNIVERSEMACHINE ([Behroozi et al. 2019](#)) to investigate the properties of galaxies in overdensities within massive halos. Since UNIVERSEMACHINE does not contain SMBH information and TRINITY does not contain star formation histories (and thus ages) of individual galaxies, we use both together. We use the empirical TRINITY model ([Zhang et al. 2023](#)) to estimate a distribution of halo masses that could host a quasar with the luminosity and SMBH mass of J0305–3150. To extract ha-

⁴ This halo mass limit roughly corresponds to an [OIII] line flux of 10^{42} erg/s, which is our 80% completeness limit. The contribution from low-mass haloes to our measured companion number counts is expected to be small due to decreasing completeness below this limit.

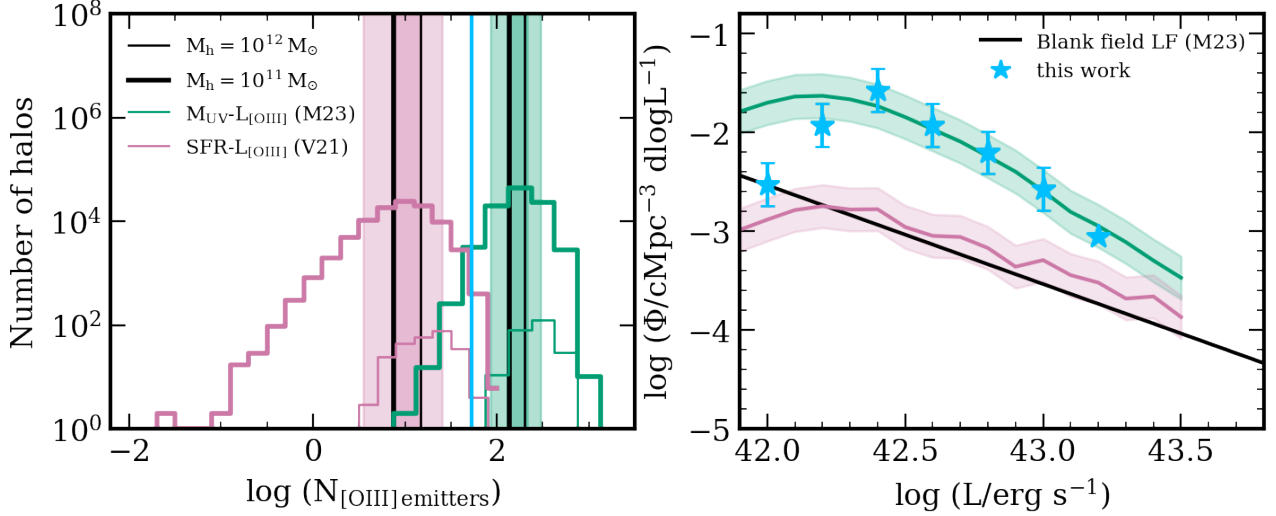


Figure 7. Predictions of [OIII]-emitting companions in $M_h > 10^{11} M_\odot$ halos extracted from UNIVERSEMACHINE (Behroozi et al. 2019). *Left:* Number of galaxies predicted in our completeness-corrected footprint, calculated by assigning $L_{[\text{OIII}]}$ based on the predicted M_{UV} (green; Matthee et al. 2023) or SFR (pink; Villa-Vélez et al. 2021), with the thick and thin histograms denoting $M_h > 10^{11} M_\odot$ and $M_h > 10^{12} M_\odot$ halos respectively. The light blue line indicates the observed number of quasar overdensity members. The black solid lines are the median predicted number counts with the shaded regions corresponding to the 1σ spread for that halo mass and [OIII] scaling relation. *Right:* Simulation-predicted [OIII] luminosity functions, with the same color scheme and 1σ errors as the left, compared to the observed LF (blue stars) and the EIGER LF (black line). The EIGER $M_{UV} - L_{[\text{OIII}]}$ relationship best predicts the observed shape in the quasar overdensity, but predicts a higher absolute number of companions at the faint end. This could be due either to suppression from the quasar or intrinsic properties of the star formation within the galaxies.

los from UNIVERSEMACHINE, we use the grism RMS footprint over the whole mosaic. We convert the RMS to a 5σ limiting line flux map by integrating a point source across a 250 km/s linewidth at $z = 6.6$. We extract 187,368 halos with $M_h > 10^{11} M_\odot$ containing overdensities of galaxies in order to assess whether the quasar halo hosts an unusual distribution of galaxies compared to other massive halos in the field. UNIVERSEMACHINE provides, among other quantities, M_{UV} and star formation histories of the simulated galaxies populating each halo.

We assign [OIII] luminosities to the extracted galaxies using two methods: one sampling the (dust-uncorrected) SFR- $L_{[\text{OIII}]}$ relation from Villa-Vélez et al. (2021) and one using the $M_{UV} - L_{[\text{OIII}]}$ relation from EIGER (Matthee et al. 2023). We find that the two

methods result in a wide spread of predicted [OIII] emitters in our footprint, with the former method predicting 7 – 25 companions with $\log(L/\text{erg s}^{-1}) > 42$ in a $M_h \sim 10^{12} M_\odot$ halo: a factor of a few below what we observe, but consistent with the blank-field luminosity function from EIGER (Figure 7). The latter method instead predicts 85 – 200 companions compared to our observed 53, which again opens the question of suppressed SFR in galaxies exposed to quasar radiation. The significant discrepancy between the predictions of these two methods likely has to do with the large scatter in the relationships between M_{UV} , [OIII] line luminosity, and instantaneous SFR as is being revealed by bursty star formation histories in both observations (Endsley et al. 2024b) and simulations (e.g., FLARES; Wilkins et al. 2023). Since UniverseMachine was calibrated on pre-JWST mea-

measurements of lower redshift galaxies with more continuous star formation, it is likely that its time resolution does not characterize the real stochasticity in these relationships.

Figure 7 shows the median theoretical [OIII] luminosity function for both methods mentioned above. We plot the LF for galaxies residing in $M_h \sim 10^{12} M_\odot$ halos after applying the same V_{\max} and completeness corrections as we did to our real data. The shape of the completeness-corrected theoretical overdensity LF measured using the EIGER M_{UV} relation closely matches what we observe in the quasar overdensity, that is, a peak in the overdensity around $\log(L/\text{erg s}^{-1}) \sim 42.3$ and a faint-end turnover. However, the turnover is weaker than what we observe. Modulo small number statistics, we might have expected only a handful more [OIII]-bright ($\log(L/\text{erg s}^{-1}) > 43$) galaxies within the quasar overdensity, so the overall paucity of observed [OIII] emitters compared to the simulation comes from the faint end.

On one hand, we posit that the grism data could be missing a real population of galaxies that are bright in the UV but have intrinsically weaker nebular emission (or patchy dust content obscuring the emission, e.g., Faisst & Morishita 2024) and scatter below our grism detection limit. On the other hand, there is substantial scatter in the scaling relations used to predict [OIII] luminosity from the simulated observables, which will particularly impact the steep faint-end of the LF. Indeed, UNIVERSEMACHINE does not capture the variance of star formation on timescales traced by [OIII] due to the coarse time resolution; thus it would not capture galaxies bright in the UV but with a recent downturn of star formation resulting in weak [OIII] emission, i.e. a departure from the canonical M_{UV} - or $SFR-L_{[\text{OIII}]}$ relationships.

6.2.2. Comparing to Costa (2024)

Distinctly, UNIVERSEMACHINE does not contain black hole physics, so our predictions do not

encode any potential baryonic effects induced by the quasars in the center of the simulated fields. We thus also compare to the simulated quasar halos from Costa (2024) who used cosmological zoom-in simulations based on the Millennium dark matter-only simulation, assuming steady-state ISM and star formation physics (Springel & Hernquist 2003) and the $L_{[\text{OIII}]} - M_h$ relation from Matthee et al. (2023). Costa (2024) considered low-mass ('LM', $0.6 - 1 \times 10^{12} M_\odot$) and high-mass ('HM', $6 - 7 \times 10^{12} M_\odot$) quasar host halos and predicted the number counts of companions with moderate ($M_* = 1 - 10 \times 10^9 M_\odot$) and high ($M_* > 10^{10} M_\odot$) mass. We can potentially rule out J0305 residing in a HM halo as, even within the variance, that study would predict tens of $M_* > 10^9 M_\odot$ and 1-10 $M_* > 10^{10} M_\odot$ companions, while we find only 9 and 0 respectively (see paper II for calculation of stellar masses); this rejection is also supported by TRINITY's prediction of a host halo mass of $\sim 1.1 \times 10^{12} M_\odot$. Yet Costa (2024) still predicts 1-10 high-mass and 4-25 moderate-mass companions even for the LM halos, while the majority of the galaxies in our sample have relatively low stellar mass (median $\log M_*/M_\odot = 8.2$; see Paper II). However, the simulation does not account for strong AGN feedback due to super-Eddington bursts and may not accurately model the dust attenuation, both of which could result in an overprediction of the number of companions. On the other hand, this also suggests that we could be missing more massive galaxies with weak nebular line emission (therefore undetectable by grism), backed up by an observed anti-correlation between stellar mass and [OIII]+H β EW (Begley et al. 2025). In this case, those galaxies can only be revealed with deeper and wider imaging bracketing the Lyman break and rest-UV/optical continuum, or ALMA observations targeting FIR lines. Alternatively, we could be still missing some physics governing the evolution of galaxies within over-

densities. Indeed, the discovery of massive [CII] companions (Decarli et al. 2018; Venemans et al. 2019) without [OIII] counterparts as well as seven LBGs consistent with the quasar redshift supports this argument.

Overall, the faintness of the [OIII] emitters and the low-mass nature of the companions in the quasar overdensity paints a picture wherein galaxies experience stochastic episodes of star formation, causing galaxies to scatter in and out of the [OIII] detection limit on the scale of 5–10 Myr (Wilkins et al. 2023; Faisst & Morishita 2024). The fact that both simulations we compare to here predict a higher population of detectable bright and massive galaxies than what is observed is puzzling, but could be explained if we are not sensitive to massive galaxies with older stars and less [OIII] emission (e.g., Looser et al. 2024, 2023). On the other hand, suppression of lower-mass halos by the central quasar engine could affect the presence of faint [OIII] emitters close to the quasar, as discussed previously. While UNIVERSEMACHINE does not resolve halos below $M_h \sim 10^{10} M_\odot$ where suppression should be strongest, the disagreement at the faint end between the observations and the simulation could be ascribed to the lack of strong quasar feedback in the simulation.

In the end, we are dealing with small number statistics in a relatively small area, and the simulations we compare to indeed predict a high amount of variance in the number of companions. The simulated [OIII] luminosities are highly sensitive to the chosen scaling relation since they are not directly predicted by the simulations, thus it is difficult to predict the absolute number of companions. A larger sample of quasars, both hosting and not hosting overdensities, is required to answer these questions, which will indeed be delivered by the full ASPIRE sample (Wang et al., in prep.; Champagne et al., in prep.)

7. CONCLUSIONS

In this work we have characterized a sample of 124 [OIII] emitters identified in the ASPIRE grism+imaging quasar legacy survey, identified over an area of 35 arcmin² surrounding the $z = 6.6$ quasar J0305–3150. 53 of these galaxies are members of a quasar-anchored protocluster at $z = 6.6$, while 18 and 20 galaxies occupy serendipitously discovered overdensities at $z = 6.2$ and $z = 5.4$. The remaining galaxies served as a field sample as a comparison between the evolution of galaxies within and without overdensities during the epoch of reionization. We found that:

- The protocluster structure suggested by in Wang et al. (2023) across 3 Mpc in a single NIRCcam pointing in fact extends over 10 Mpc within a 35 arcmin² mosaic. The 53 galaxies at $6.5 < z < 6.8$ represent an overdensity of $\delta_{\text{gal}} = 12.5 \pm 2.6$. They are distinctly distributed along filaments extending down the line of sight from the quasar.
- The [OIII] luminosity function in the quasar protocluster has a distinct peak at $\log(L/\text{erg s}^{-1}) = 42.3$, with a faint-end turnover that is not due to incompleteness. We suggest that we are missing a population of galaxies with [OIII] emission just below the grism detection limit since bursty star formation will affect the strength of [OIII] emission on very short (tens of Myr) timescales.
- There is a dearth of [OIII] emitters within 80 ckpc from the quasar while there are three massive [CII] emitters and an LAE; we suggest that this could be due to mergers with the host galaxy, dust extinction, and/or mild suppression of low-mass [OIII] emitters due to photoionization heating from the quasar.
- After computing the quasar host halo mass from TRINITY, we compare our

[OIII] flux distribution with galaxies in similar halos extracted from UNIVERSEMACHINE and a hydrodynamic zoom-in simulation from Costa (2024). The number of companion galaxies is very sensitive to the scaling relation used to paint on [OIII] luminosity, but our results are consistent with the protocluster overdensity being weaker than expected. This supports our argument that galaxies with stochastic SFHs are not picked up by this survey and would appear as LBGs with no line emission in a dedicated photometric survey. Indeed, a subset of our NIRCам data is covered by *HST* which shows 7 LBGs without [OIII] counterparts but with photometric redshifts consistent with the protocluster; further multiwavelength imaging would be required across the full mosaic field of view to confirm this trend at larger distances.

A larger quasar sample will be presented in future ASPIRE publications which will help build up population statistics for quasar environments. Wang et al. (in prep.) will present the ALMA counterpart to ASPIRE which includes mosaicked 1.1 arcmin \times 1.1 arcmin Band 6 data in this field targeting dust continuum and [CII]. In future studies, it will be crucial to obtain better photometric coverage of the rest-optical and NIR emission of many ASPIRE fields, especially through NIRCам medium bands and/or MIRI broadband photometry to probe low-sSFR galaxies not detectable by the grism spectroscopy. It will also be interesting to compare the population of [OIII] emitters with a follow-up sample of Ly α emitters in the same field to assess the correlations between Ly α enhancement and high nebular line EW. Paper II (Champagne et al. 2024) presents detailed SED fitting and an environmental analysis of the [OIII] emitters identified in this field.

JBC acknowledges funding from the JWST Arizona/Steward Postdoc in Early galaxies and Reionization (JASPER) Scholar contract at the University of Arizona. FW and JBC acknowledge support from NSF Grant AST-2308258. CM acknowledges support from Fondecyt Iniciacion grant 11240336 and ANID BASAL project FB210003. FL acknowledges support from the INAF GO 2022 grant “The birth of the giants: JWST sheds light on the build-up of quasars at cosmic dawn” and from the INAF 2023 mini-grant “Exploiting the powerful capabilities of JWST/NIRSpec to unveil the distant Universe.” AL acknowledges support by the PRIN MUR “2022935STW.” SZ acknowledges support from the National Science Foundation of China (grant no. 12303011). SEIB is supported by the Deutsche Forschungsgemeinschaft (DFG) under Emmy Noether grant number BO 5771/1-1. MT acknowledges support from the NWO grant 016.VIDI.189.162 (“ODIN”).

This work is based on observations made with the NASA/ESA/CSA James Webb Space Telescope. The data were obtained from the Mikulski Archive for Space Telescopes at the Space Telescope Science Institute, which is operated by the Association of Universities for Research in Astronomy, Inc., under NASA contract NAS 5-03127 for JWST. These observations are associated with programs #2078 and #3225. Support for these programs was given through a grant from the Space Telescope Science Institute, which is operated by the Association of Universities for Research in Astronomy, Inc., under NASA contract NAS 5-03127. The specific observations analyzed can be accessed via [10.17909/vt74-kd84](https://doi.org/10.17909/vt74-kd84).

Software: Astropy (Astropy Collaboration et al. 2013, 2018, 2022), SourceXtractor++ (Bertin et al. 2020)

Table 1. Observational properties of [OIII] emitters in the protocluster. The sources are in the order they appear in the photometric detection catalog, with J0305-O3E-PC standing for J0305M3150-[OIII] emitter-protocluster member. The [OIII]-derived redshift is assumed to have an uncertainty of $\delta z = 0.003$. All equivalent widths are in the rest frame, using the line-subtracted F356W photometry as the continuum.

Name	RA (J2000)	Dec (J2000)	z	$\log L_{[\text{OIII}]}$ $10^{42} \text{ erg s}^{-1}$	$\text{EW}_{[\text{OIII}]}$ \AA	$\text{EW}_{[\text{OIII}]+\text{H}\beta}$ \AA
J0305-O3E-PC-001	03:05:28.955	-31:48:55.22	6.616	9.33 ± 0.92	423 ± 50	649 ± 54
J0305-O3E-PC-002	03:05:28.724	-31:49:19.32	6.615	6.66 ± 0.77	310 ± 98	444 ± 103
J0305-O3E-PC-003	03:05:28.463	-31:49:26.41	6.621	6.90 ± 0.66	452 ± 224	737 ± 247
J0305-O3E-PC-004	03:05:27.846	-31:48:58.42	6.616	10.96 ± 0.86	406 ± 87	681 ± 96
J0305-O3E-PC-005	03:05:27.226	-31:49:28.47	6.625	2.06 ± 0.81	119 ± 35	192 ± 36
J0305-O3E-PC-006	03:05:26.887	-31:49:23.75	6.614	3.85 ± 0.70	326 ± 123	425 ± 128
J0305-O3E-PC-007	03:05:26.828	-31:49:59.19	6.618	2.88 ± 0.93	198 ± 24	378 ± 26
J0305-O3E-PC-008	03:05:25.235	-31:50:10.56	6.621	3.18 ± 0.88	123 ± 34	301 ± 37
J0305-O3E-PC-009	03:05:24.442	-31:49:15.83	6.614	1.84 ± 0.79	518 ± 166	907 ± 191
J0305-O3E-PC-010	03:05:25.373	-31:50:57.16	6.628	18.14 ± 0.91	411 ± 50	639 ± 55
J0305-O3E-PC-011	03:05:23.246	-31:47:32.68	6.611	4.70 ± 0.67	498 ± 195	616 ± 202
J0305-O3E-PC-012	03:05:24.732	-31:50:13.34	6.623	3.53 ± 0.78	350 ± 123	617 ± 135
J0305-O3E-PC-013	03:05:24.657	-31:50:25.01	6.579	1.39 ± 0.86	577 ± 97	742 ± 103
J0305-O3E-PC-014	03:05:22.216	-31:48:02.45	6.609	2.32 ± 0.83	238 ± 58	361 ± 60
J0305-O3E-PC-015	03:05:22.893	-31:50:12.74	6.622	1.10 ± 0.83	197 ± 44	258 ± 45
J0305-O3E-PC-016	03:05:21.698	-31:49:36.02	6.615	3.46 ± 1.00	479 ± 7	745 ± 12
J0305-O3E-PC-017	03:05:21.478	-31:49:23.91	6.617	3.71 ± 0.90	349 ± 50	504 ± 53
J0305-O3E-PC-018	03:05:21.403	-31:49:19.96	6.615	2.22 ± 1.00	247 ± 3	420 ± 5
J0305-O3E-PC-019	03:05:21.786	-31:49:52.57	6.621	10.18 ± 0.92	280 ± 33	457 ± 35
J0305-O3E-PC-020	03:05:21.820	-31:50:25.36	6.617	2.64 ± 1.00	319 ± 5	582 ± 10
J0305-O3E-PC-021	03:05:22.445	-31:51:35.27	6.652	3.06 ± 1.00	357 ± 6	639 ± 12
J0305-O3E-PC-022	03:05:21.222	-31:49:59.74	6.617	4.94 ± 0.77	459 ± 154	720 ± 169
J0305-O3E-PC-023	03:05:20.596	-31:49:10.13	6.616	4.52 ± 0.91	375 ± 51	660 ± 57
J0305-O3E-PC-024	03:05:21.041	-31:49:58.66	6.618	6.06 ± 0.75	340 ± 129	544 ± 139
J0305-O3E-PC-025	03:05:21.049	-31:49:58.98	6.612	6.61 ± 0.88	258 ± 40	359 ± 42
J0305-O3E-PC-026	03:05:20.424	-31:49:11.65	6.612	3.79 ± 0.80	362 ± 113	605 ± 123
J0305-O3E-PC-027	03:05:18.900	-31:48:11.61	6.609	5.95 ± 0.87	604 ± 101	840 ± 110
J0305-O3E-PC-028	03:05:19.997	-31:50:19.68	6.619	1.91 ± 0.70	101 ± 37	123 ± 37
J0305-O3E-PC-029	03:05:19.972	-31:50:19.58	6.616	3.95 ± 0.71	183 ± 62	214 ± 63
J0305-O3E-PC-030	03:05:19.955	-31:50:19.26	6.624	2.44 ± 0.84	109 ± 25	157 ± 25
J0305-O3E-PC-031	03:05:19.735	-31:51:38.81	6.74	2.34 ± 0.83	319 ± 82	507 ± 88
J0305-O3E-PC-032	03:05:18.612	-31:50:10.65	6.54	3.89 ± 1.00	453 ± 7	836 ± 14
J0305-O3E-PC-033	03:05:18.717	-31:50:38.77	6.619	4.42 ± 1.00	204 ± 2	450 ± 6
J0305-O3E-PC-034	03:05:18.729	-31:50:38.53	6.616	3.99 ± 0.71	237 ± 95	339 ± 98
J0305-O3E-PC-035	03:05:18.499	-31:50:41.23	6.615	3.70 ± 0.90	326 ± 62	672 ± 71

Table 2. Table 1 continued.

Name	RA	Dec	z	$\log L_{[OIII]}$ $10^{42} \text{ erg s}^{-1}$	$EW_{[OIII]}$ \AA	$EW_{[OIII]+H\beta}$ \AA
J0305-O3E-PC-036	03:05:16.291	-31:49:32.29	6.599	2.42 ± 0.76	154 ± 58	253 ± 60
J0305-O3E-PC-037	03:05:17.110	-31:50:58.24	6.632	4.15 ± 0.81	314 ± 82	460 ± 86
J0305-O3E-PC-038	03:05:16.530	-31:50:22.65	6.667	10.79 ± 0.85	280 ± 63	462 ± 67
J0305-O3E-PC-039	03:05:16.794	-31:50:57.26	6.628	8.33 ± 0.91	513 ± 70	845 ± 79
J0305-O3E-PC-040	03:05:15.698	-31:50:37.57	6.616	3.29 ± 0.88	585 ± 116	1213 ± 144
J0305-O3E-PC-041	03:05:16.824	-31:53:27.01	6.503	6.85 ± 0.89	561 ± 84	852 ± 92
J0305-O3E-PC-042	03:05:14.691	-31:53:20.93	6.549	3.72 ± 0.90	435 ± 71	798 ± 82
J0305-O3E-PC-043	03:05:13.138	-31:52:52.45	6.67	3.25 ± 0.76	260 ± 72	303 ± 73
J0305-O3E-PC-044	03:05:11.209	-31:49:43.71	6.648	3.45 ± 0.77	308 ± 94	434 ± 98
J0305-O3E-PC-045	03:05:10.353	-31:49:04.97	6.815	4.47 ± 0.82	627 ± 146	834 ± 157
J0305-O3E-PC-046	03:05:10.411	-31:49:12.04	6.627	3.56 ± 0.89	408 ± 65	648 ± 71
J0305-O3E-PC-047	03:05:12.580	-31:52:52.76	6.673	7.38 ± 1.00	467 ± 7	718 ± 12
J0305-O3E-PC-048	03:05:12.990	-31:53:57.53	6.599	5.88 ± 0.93	441 ± 52	937 ± 65
J0305-O3E-PC-049	03:05:10.165	-31:49:11.53	6.755	3.68 ± 0.78	268 ± 69	316 ± 70
J0305-O3E-PC-050	03:05:11.348	-31:52:17.67	6.517	3.55 ± 0.90	1894 ± 279	3770 ± 451
J0305-O3E-PC-051	03:05:10.246	-31:52:00.90	6.596	5.99 ± 1.00	205 ± 2	306 ± 3
J0305-O3E-PC-052	03:05:11.455	-31:54:02.57	6.593	4.80 ± 1.00	523 ± 7	728 ± 11
J0305-O3E-PC-053	03:05:07.985	-31:49:11.78	6.748	3.16 ± 1.00	300 ± 5	492 ± 8

APPENDIX

A. EXAMPLE GRISM SPECTRUM

Here we display a representative example of one of our grism spectra, source #7025 at $z = 6.54$, demonstrating the quality of our high-confidence [OIII] emitters in Figure 8.

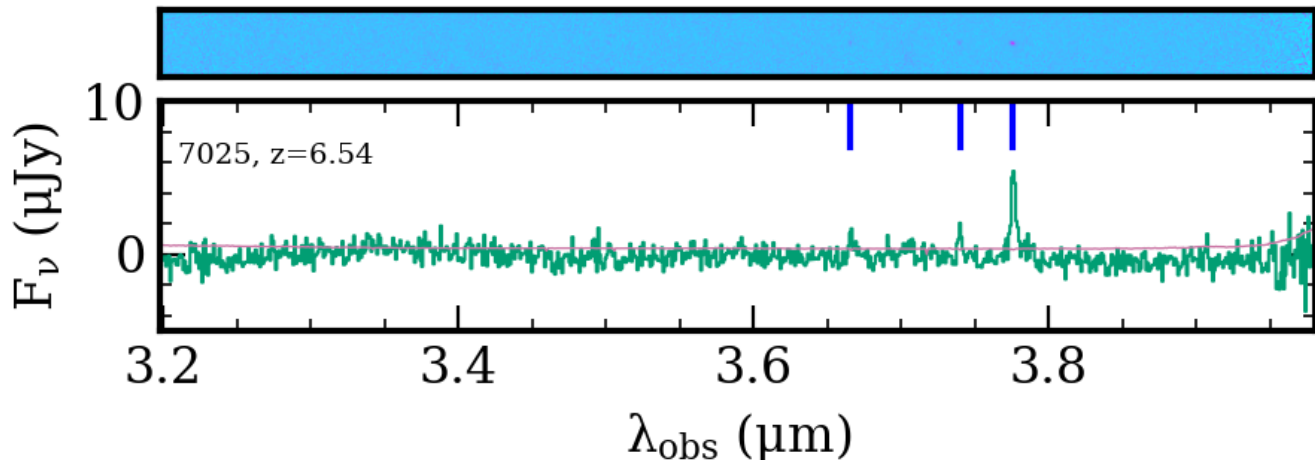


Figure 8. NIRCam/WFSS grism spectrum of source #7025 at $z = 6.54$. *Top:* 2D continuum-subtracted spectrum of the source. *Bottom:* The 1D optimally-extracted spectrum in green, with the error vector displayed in pink. Vertical blue lines indicate the locations of H β , [OIII] λ 4959 and [OIII] λ 5007, which are all securely detected. All galaxies in our sample have a secure detection of the [OIII] doublet.

B. UNDETECTED LBGs

In §3 we discussed matching the LBG catalog from Champagne et al. (2023) to the [OIII] catalog presented here, most of which are now either spectroscopically confirmed or eliminated as interlopers based on updated photometric redshifts. However, three LBGs from Champagne et al. (2023) are not detected in the F356W image so no spectrum was extracted for them. Champagne et al. (2023) groups the *HST*-detected LBGs into “secure” and “marginal” samples, where the “secure” sample must satisfy: 1) the photometric redshift PDF $P(z)$ contains an 80% probability of lying at $z > 6$, 2) be detected in both F125W and F160W with $> 5\sigma$ significance, and 3) displays a non-detection in F606W. For the “marginal” case, this requirement is relaxed to $> 40\%$ of $P(z)$ contained at $z > 6$ and a 3σ detection in F125W and F160W. As can be seen in Figure 9, source #2109 is likely not detected in F356W due to deblending from the nearby southern source. Source #28 is of low significance ($\sim 4\sigma$) even in F160W, and does not appear visible in F356W. Finally, source #4783 is also probably picked up as an extended feature of the brighter northern source. Since all three LBGs were in the “marginal” sample, we disregard them as candidates in the F356W catalog.

REFERENCES

Angulo, R. E., Springel, V., White, S. D. M., et al. 2012, MNRAS, 425, 2722, doi: 10.1111/j.1365-2966.2012.21783.x

Arita, J., Kashikawa, N., Matsuoka, Y., et al. 2023, ApJ, 954, 210, doi: 10.3847/1538-4357/ace43a

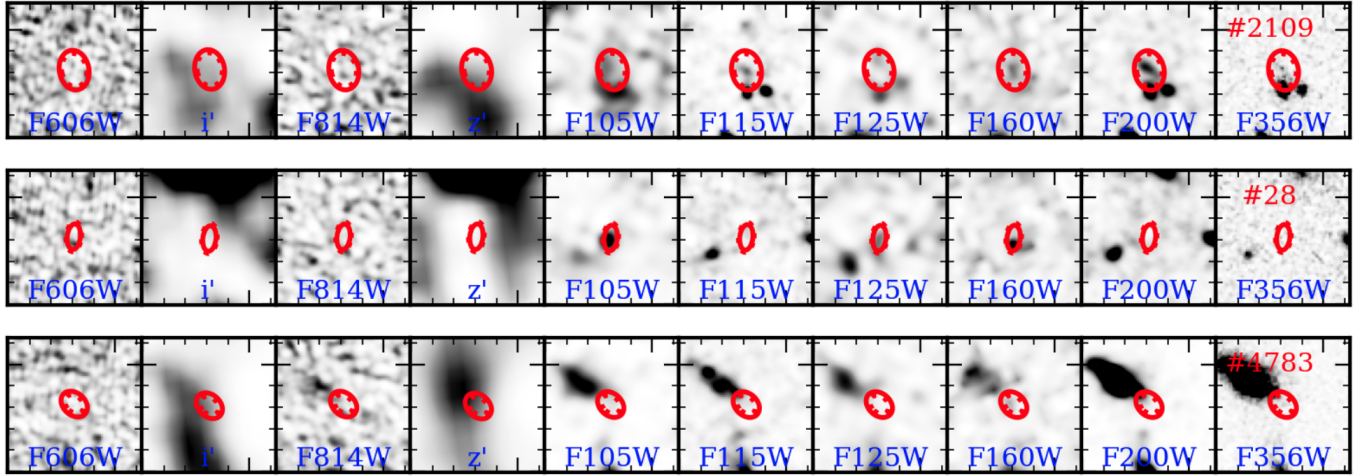


Figure 9. Cutouts in Subaru i' , z , *HST*/ACS and WFC3 F606W, F814W, F105W, F125W, F160W, and *JWST*/NIRCam F115W, F200W, F356W displayed in wavelength order. Cutouts are $2'' \times 2''$, and the aperture used for photometry in the F160W detection image is displayed in red. All three sources shown are classified as “marginal” LBGs by Champagne et al. (2023) and are discarded in the present F356W sample.

- Astropy Collaboration, Robitaille, T. P., Tollerud, E. J., et al. 2013, *A&A*, 558, A33, doi: [10.1051/0004-6361/201322068](https://doi.org/10.1051/0004-6361/201322068)
- Astropy Collaboration, Price-Whelan, A. M., Sipőcz, B. M., et al. 2018, *AJ*, 156, 123, doi: [10.3847/1538-3881/aabc4f](https://doi.org/10.3847/1538-3881/aabc4f)
- Astropy Collaboration, Price-Whelan, A. M., Lim, P. L., et al. 2022, *ApJ*, 935, 167, doi: [10.3847/1538-4357/ac7c74](https://doi.org/10.3847/1538-4357/ac7c74)
- Bañados, E., Venemans, B., Walter, F., et al. 2013, *ApJ*, 773, 178, doi: [10.1088/0004-637X/773/2/178](https://doi.org/10.1088/0004-637X/773/2/178)
- Bañados, E., Venemans, B. P., Decarli, R., et al. 2016, *ApJS*, 227, 11, doi: [10.3847/0067-0049/227/1/11](https://doi.org/10.3847/0067-0049/227/1/11)
- Bañados, E., Schindler, J.-T., Venemans, B. P., et al. 2023, *ApJS*, 265, 29, doi: [10.3847/1538-4365/acb3c7](https://doi.org/10.3847/1538-4365/acb3c7)
- Begley, R., McLure, R. J., Cullen, F., et al. 2025, *MNRAS*, doi: [10.1093/mnras/staf211](https://doi.org/10.1093/mnras/staf211)
- Behroozi, P., Wechsler, R. H., Hearin, A. P., & Conroy, C. 2019, *MNRAS*, 488, 3143, doi: [10.1093/mnras/stz1182](https://doi.org/10.1093/mnras/stz1182)
- Bertin, E., Schefer, M., Apostolakos, N., et al. 2020, in *Astronomical Society of the Pacific Conference Series*, Vol. 527, *Astronomical Data Analysis Software and Systems XXIX*, ed. R. Pizzo, E. R. Deul, J. D. Mol, J. de Plaa, & H. Verkouter, 461
- Bosman, S. E. I., Kakiichi, K., Meyer, R. A., et al. 2020, *ApJ*, 896, 49, doi: [10.3847/1538-4357/ab85cd](https://doi.org/10.3847/1538-4357/ab85cd)
- Boyett, K., Bunker, A. J., Curtis-Lake, E., et al. 2024, *MNRAS*, 535, 1796, doi: [10.1093/mnras/stae2430](https://doi.org/10.1093/mnras/stae2430)
- Brammer, G. B., van Dokkum, P. G., & Coppi, P. 2008, *ApJ*, 686, 1503, doi: [10.1086/591786](https://doi.org/10.1086/591786)
- Champagne, J. B., Casey, C. M., Finkelstein, S. L., et al. 2023, *ApJ*, 952, 99, doi: [10.3847/1538-4357/acda8d](https://doi.org/10.3847/1538-4357/acda8d)
- Champagne, J. B., Decarli, R., Casey, C. M., et al. 2018, *ApJ*, 867, 153, doi: [10.3847/1538-4357/aae396](https://doi.org/10.3847/1538-4357/aae396)
- Champagne, J. B., Wang, F., Yang, J., et al. 2024, arXiv e-prints, arXiv:2410.03827, doi: [10.48550/arXiv.2410.03827](https://doi.org/10.48550/arXiv.2410.03827)
- Chen, H. 2020, *ApJ*, 893, 165, doi: [10.3847/1538-4357/ab80c6](https://doi.org/10.3847/1538-4357/ab80c6)
- Chiang, Y.-K., Overzier, R. A., Gebhardt, K., & Henriques, B. 2017, *ApJL*, 844, L23, doi: [10.3847/2041-8213/aa7e7b](https://doi.org/10.3847/2041-8213/aa7e7b)
- Costa, T. 2024, *MNRAS*, 531, 930, doi: [10.1093/mnras/stae1157](https://doi.org/10.1093/mnras/stae1157)
- Costa, T., Sijacki, D., Trenti, M., & Haehnelt, M. G. 2014, *MNRAS*, 439, 2146, doi: [10.1093/mnras/stu101](https://doi.org/10.1093/mnras/stu101)
- Cucciati, O., Lemaux, B. C., Zamorani, G., et al. 2018, *A&A*, 619, A49, doi: [10.1051/0004-6361/201833655](https://doi.org/10.1051/0004-6361/201833655)

- Dannerbauer, H., Kurk, J. D., De Breuck, C., et al. 2014, *A&A*, 570, A55, doi: [10.1051/0004-6361/201423771](https://doi.org/10.1051/0004-6361/201423771)
- Decarli, R., Walter, F., Venemans, B. P., et al. 2018, *ApJ*, 854, 97, doi: [10.3847/1538-4357/aaa5aa](https://doi.org/10.3847/1538-4357/aaa5aa)
- Di Matteo, T., Croft, R. A. C., Feng, Y., Waters, D., & Wilkins, S. 2017, *MNRAS*, 467, 4243, doi: [10.1093/mnras/stx319](https://doi.org/10.1093/mnras/stx319)
- Eilers, A.-C., Mackenzie, R., Pizzati, E., et al. 2024, *ApJ*, 974, 275, doi: [10.3847/1538-4357/ad778b](https://doi.org/10.3847/1538-4357/ad778b)
- Eldridge, J. J., & Stanway, E. R. 2022, *ARA&A*, 60, 455, doi: [10.1146/annurev-astro-052920-100646](https://doi.org/10.1146/annurev-astro-052920-100646)
- Endsley, R., Chisholm, J., Stark, D. P., Topping, M. W., & Whitler, L. 2024a, arXiv e-prints, arXiv:2410.01905, doi: [10.48550/arXiv.2410.01905](https://doi.org/10.48550/arXiv.2410.01905)
- Endsley, R., Stark, D. P., Chevallard, J., & Charlot, S. 2021, *MNRAS*, 500, 5229, doi: [10.1093/mnras/staa3370](https://doi.org/10.1093/mnras/staa3370)
- Endsley, R., Stark, D. P., Whitler, L., et al. 2023a, *MNRAS*, 524, 2312, doi: [10.1093/mnras/stad1919](https://doi.org/10.1093/mnras/stad1919)
- . 2023b, arXiv e-prints, arXiv:2306.05295, doi: [10.48550/arXiv.2306.05295](https://doi.org/10.48550/arXiv.2306.05295)
- . 2024b, *MNRAS*, 533, 1111, doi: [10.1093/mnras/stae1857](https://doi.org/10.1093/mnras/stae1857)
- Faisst, A. L., & Morishita, T. 2024, *ApJ*, 971, 47, doi: [10.3847/1538-4357/ad58e2](https://doi.org/10.3847/1538-4357/ad58e2)
- Fan, X., Bañados, E., & Simcoe, R. A. 2023, *ARA&A*, 61, 373, doi: [10.1146/annurev-astro-052920-102455](https://doi.org/10.1146/annurev-astro-052920-102455)
- Farina, E. P., Venemans, B. P., Decarli, R., et al. 2017, *ApJ*, 848, 78, doi: [10.3847/1538-4357/aa8df4](https://doi.org/10.3847/1538-4357/aa8df4)
- Finkelstein, S. L. 2016, *PASA*, 33, e037, doi: [10.1017/pasa.2016.26](https://doi.org/10.1017/pasa.2016.26)
- Finkelstein, S. L., Ryan, Russell E., J., Papovich, C., et al. 2015, *ApJ*, 810, 71, doi: [10.1088/0004-637X/810/1/71](https://doi.org/10.1088/0004-637X/810/1/71)
- Gaia Collaboration. 2020, *VizieR Online Data Catalog*, I/350
- García-Vergara, C., Hennawi, J. F., Barrientos, L. F., & Rix, H.-W. 2017, *ApJ*, 848, 7, doi: [10.3847/1538-4357/aa8b69](https://doi.org/10.3847/1538-4357/aa8b69)
- Hill, R., Chapman, S., Scott, D., et al. 2020, *MNRAS*, 495, 3124, doi: [10.1093/mnras/staa1275](https://doi.org/10.1093/mnras/staa1275)
- Kashikawa, N., Kitayama, T., Doi, M., et al. 2007, *ApJ*, 663, 765, doi: [10.1086/518410](https://doi.org/10.1086/518410)
- Kashino, D., Lilly, S. J., Matthee, J., et al. 2023, *ApJ*, 950, 66, doi: [10.3847/1538-4357/acc588](https://doi.org/10.3847/1538-4357/acc588)
- Kim, S., Stiavelli, M., Trenti, M., et al. 2009, *ApJ*, 695, 809, doi: [10.1088/0004-637X/695/2/809](https://doi.org/10.1088/0004-637X/695/2/809)
- Klypin, A., Yepes, G., Gottlöber, S., Prada, F., & Heß, S. 2016, *MNRAS*, 457, 4340, doi: [10.1093/mnras/stw248](https://doi.org/10.1093/mnras/stw248)
- Lambert, T. S., Assef, R. J., Mazzucchelli, C., et al. 2024, *A&A*, 689, A331, doi: [10.1051/0004-6361/202449566](https://doi.org/10.1051/0004-6361/202449566)
- Looser, T. J., D'Eugenio, F., Maiolino, R., et al. 2023, arXiv e-prints, arXiv:2306.02470, doi: [10.48550/arXiv.2306.02470](https://doi.org/10.48550/arXiv.2306.02470)
- . 2024, *Nature*, 629, 53, doi: [10.1038/s41586-024-07227-0](https://doi.org/10.1038/s41586-024-07227-0)
- Lupi, A., Quadri, G., Volonteri, M., Colpi, M., & Regan, J. A. 2024, *A&A*, 686, A256, doi: [10.1051/0004-6361/202348788](https://doi.org/10.1051/0004-6361/202348788)
- Lupi, A., Volonteri, M., Decarli, R., Bovino, S., & Silk, J. 2022, *MNRAS*, 510, 5760, doi: [10.1093/mnras/stac014](https://doi.org/10.1093/mnras/stac014)
- Matthee, J., Mackenzie, R., Simcoe, R. A., et al. 2023, *ApJ*, 950, 67, doi: [10.3847/1538-4357/acc846](https://doi.org/10.3847/1538-4357/acc846)
- Mazzucchelli, C., Bañados, E., Decarli, R., et al. 2017a, *ApJ*, 834, 83, doi: [10.3847/1538-4357/834/1/83](https://doi.org/10.3847/1538-4357/834/1/83)
- Mazzucchelli, C., Bañados, E., Venemans, B. P., et al. 2017b, *ApJ*, 849, 91, doi: [10.3847/1538-4357/aa9185](https://doi.org/10.3847/1538-4357/aa9185)
- Mazzucchelli, C., Bischetti, M., D'Odorico, V., et al. 2023, *A&A*, 676, A71, doi: [10.1051/0004-6361/202346317](https://doi.org/10.1051/0004-6361/202346317)
- Meyer, R. A., Decarli, R., Walter, F., et al. 2022, *ApJ*, 927, 141, doi: [10.3847/1538-4357/ac4f67](https://doi.org/10.3847/1538-4357/ac4f67)
- Muldrew, S. I., Hatch, N. A., & Cooke, E. A. 2015, *MNRAS*, 452, 2528, doi: [10.1093/mnras/stv1449](https://doi.org/10.1093/mnras/stv1449)
- Ota, K., Venemans, B. P., Taniguchi, Y., et al. 2018, *ApJ*, 856, 109, doi: [10.3847/1538-4357/aab35b](https://doi.org/10.3847/1538-4357/aab35b)
- Overzier, R. A. 2016, *A&A Rv*, 24, 14, doi: [10.1007/s00159-016-0100-3](https://doi.org/10.1007/s00159-016-0100-3)
- Overzier, R. A., Guo, Q., Kauffmann, G., et al. 2009, *MNRAS*, 394, 577, doi: [10.1111/j.1365-2966.2008.14264.x](https://doi.org/10.1111/j.1365-2966.2008.14264.x)

- Pensabene, A., Cantalupo, S., Cicone, C., et al. 2024, *A&A*, 684, A119, doi: [10.1051/0004-6361/202348659](https://doi.org/10.1051/0004-6361/202348659)
- Rennehan, D., Babul, A., Hayward, C. C., et al. 2020, *MNRAS*, 493, 4607, doi: [10.1093/mnras/staa541](https://doi.org/10.1093/mnras/staa541)
- Rojas-Ruiz, S., Mazzucchelli, C., Finkelstein, S. L., et al. 2024, *ApJ*, 967, 27, doi: [10.3847/1538-4357/ad3bab](https://doi.org/10.3847/1538-4357/ad3bab)
- Satyavolu, S., Kulkarni, G., Keating, L. C., & Haehnelt, M. G. 2023, *MNRAS*, 521, 3108, doi: [10.1093/mnras/stad729](https://doi.org/10.1093/mnras/stad729)
- Springel, V., & Hernquist, L. 2003, *MNRAS*, 339, 289, doi: [10.1046/j.1365-8711.2003.06206.x](https://doi.org/10.1046/j.1365-8711.2003.06206.x)
- Sun, F., Egami, E., Pirzkal, N., et al. 2023, *ApJ*, 953, 53, doi: [10.3847/1538-4357/acd53c](https://doi.org/10.3847/1538-4357/acd53c)
- Toshikawa, J., Wuyts, S., Kashikawa, N., et al. 2024, *MNRAS*, 527, 6276, doi: [10.1093/mnras/stad3162](https://doi.org/10.1093/mnras/stad3162)
- Trenti, M., & Stiavelli, M. 2008, *ApJ*, 676, 767, doi: [10.1086/528674](https://doi.org/10.1086/528674)
- Trussler, J. A. A., Conselice, C. J., Adams, N., et al. 2025, *MNRAS*, doi: [10.1093/mnras/staf213](https://doi.org/10.1093/mnras/staf213)
- Venemans, B. P., Neeleman, M., Walter, F., et al. 2019, *ApJL*, 874, L30, doi: [10.3847/2041-8213/ab11cc](https://doi.org/10.3847/2041-8213/ab11cc)
- Venemans, B. P., Walter, F., Zschaechner, L., et al. 2016, *ApJ*, 816, 37, doi: [10.3847/0004-637X/816/1/37](https://doi.org/10.3847/0004-637X/816/1/37)
- Venemans, B. P., Findlay, J. R., Sutherland, W. J., et al. 2013, *ApJ*, 779, 24, doi: [10.1088/0004-637X/779/1/24](https://doi.org/10.1088/0004-637X/779/1/24)
- Venemans, B. P., Walter, F., Neeleman, M., et al. 2020, *ApJ*, 904, 130, doi: [10.3847/1538-4357/abc563](https://doi.org/10.3847/1538-4357/abc563)
- Villa-Vélez, J. A., Buat, V., Theulé, P., Boquien, M., & Burgarella, D. 2021, *A&A*, 654, A153, doi: [10.1051/0004-6361/202140890](https://doi.org/10.1051/0004-6361/202140890)
- Volonteri, M., Habouzit, M., & Colpi, M. 2021, *Nature Reviews Physics*, 3, 732, doi: [10.1038/s42254-021-00364-9](https://doi.org/10.1038/s42254-021-00364-9)
- Wang, F., Fan, X., Yang, J., et al. 2021, *ApJ*, 908, 53, doi: [10.3847/1538-4357/abcc5e](https://doi.org/10.3847/1538-4357/abcc5e)
- Wang, F., Yang, J., Hennawi, J. F., et al. 2023, *ApJL*, 951, L4, doi: [10.3847/2041-8213/accd6f](https://doi.org/10.3847/2041-8213/accd6f)
- Whitler, L., Stark, D. P., Endsley, R., et al. 2023, *MNRAS*, 519, 5859, doi: [10.1093/mnras/stad004](https://doi.org/10.1093/mnras/stad004)
- Wilkins, S. M., Lovell, C. C., Vijayan, A. P., et al. 2023, *MNRAS*, 522, 4014, doi: [10.1093/mnras/stad1126](https://doi.org/10.1093/mnras/stad1126)
- Yang, J., Wang, F., Fan, X., et al. 2019, *AJ*, 157, 236, doi: [10.3847/1538-3881/ab1be1](https://doi.org/10.3847/1538-3881/ab1be1)
- . 2023, *ApJL*, 951, L5, doi: [10.3847/2041-8213/acc9c8](https://doi.org/10.3847/2041-8213/acc9c8)
- Zana, T., Carniani, S., Prelogović, D., et al. 2023, *A&A*, 679, A77, doi: [10.1051/0004-6361/202347172](https://doi.org/10.1051/0004-6361/202347172)
- Zhang, H., Behroozi, P., Volonteri, M., et al. 2023, *MNRAS*, 518, 2123, doi: [10.1093/mnras/stac2633](https://doi.org/10.1093/mnras/stac2633)
- . 2024, *MNRAS*, 531, 4974, doi: [10.1093/mnras/stae1447](https://doi.org/10.1093/mnras/stae1447)

All Authors and Affiliations

JACLYN B. CHAMPAGNE,¹ FEIGE WANG,^{1,2} HAOWEN ZHANG (张昊文),¹ JINYI YANG,^{1,2}
XIAOHUI FAN,¹ JOSEPH F. HENNAWI,³ FENGWU SUN,¹ EDUARDO BAÑADOS,⁴ SARAH E. I. BOSMAN,^{5,6}
TIAGO COSTA,⁷ ANNA-CHRISTINA EILERS,^{8,9} RYAN ENDSLEY,¹⁰ XIANGYU JIN,¹ HYUNSUNG D. JUN,¹¹
MINGYU LI,¹² XIAOJING LIN,¹ WEIZHE LIU,¹ FEDERICA LOIACONO,¹³ ALESSANDRO LUPI,^{14,15,16}
CHIARA MAZZUCHELLI,¹⁷ MARIA PUDOKA,¹ KLAUDIA PROTUŠOVÀ,^{5,6} SOFÍA ROJAS-RUIZ,¹⁸
WEI LEONG TEE,¹ MAXIME TREBITSCH,¹⁹ BRAM P. VENEMANS,²⁰ MING-YANG ZHUANG (庄明阳),²¹
AND SIWEI ZOU²²

¹*Steward Observatory, University of Arizona, 933 N. Cherry Ave, Tucson, AZ 85721, USA*

²*Department of Astronomy, University of Michigan, 1085 S. University Ave., Ann Arbor, MI 48109, USA*

³*Department of Physics, University of California, Santa Barbara, CA 93106-9530, USA*

⁴*Max Planck Institut für Astronomie, Königstuhl 17, D-69117, Heidelberg, Germany*

⁵*Institute for Theoretical Physics, Heidelberg University, Philosophenweg 12, D-69120, Heidelberg, Germany*

⁶*Max-Planck-Institut für Astronomie, Königstuhl 17, 69117 Heidelberg, Germany*

⁷*School of Mathematics, Statistics and Physics, Newcastle University, Newcastle upon Tyne, NE1 7RU, UK*

⁸*Department of Physics, Massachusetts Institute of Technology, Cambridge, MA 02139, USA*

⁹*MIT Kavli Institute for Astrophysics and Space Research, Massachusetts Institute of Technology, Cambridge, MA 02139, USA*

¹⁰*Department of Astronomy, University of Texas Austin, 2515 Speedway Blvd, Austin, TX 78712, USA*

¹¹*Department of Physics, Northwestern College, 101 7th St SW, Orange City, IA 51041, USA*

¹²*Department of Astronomy, Tsinghua University, Beijing 100084, China*

¹³*INAF - Osservatorio di Astrofisica e Scienza dello Spazio di Bologna, via Gobetti 93/3, I-40129, Bologna, Italy*

¹⁴*Dipartimento di Scienza e Alta Tecnologia, Università degli Studi dell'Insubria, via Valleggio 11, I-22100, Como, Italy*

¹⁵*INFN, Sezione di Milano-Bicocca, Piazza della Scienza 3, I-20126 Milano, Italy*

¹⁶*Dipartimento di Fisica "G. Occhialini", Università degli Studi di Milano-Bicocca, Piazza della Scienza 3, I-20126 Milano, Italy*

¹⁷*Instituto de Estudios Astrofísicos, Facultad de Ingeniería y Ciencias, Universidad Diego Portales, Avenida Ejercito Libertador 441, Santiago, Chile*

¹⁸*Department of Physics and Astronomy, University of California, Los Angeles, 430 Portola Plaza, Los Angeles, CA 90095, USA*

¹⁹*Kapteyn Astronomical Institute, University of Groningen, P.O Box 800, 9700 AV Groningen, The Netherlands*

²⁰*Leiden Observatory, Leiden University, Einsteinweg 55, NL-2333 CC Leiden, the Netherlands*

²¹*Department of Astronomy, University of Illinois Urbana-Champaign, Urbana, IL 61801, USA*

²²*Chinese Academy of Sciences South America Center for Astronomy, National Astronomical Observatories, CAS, Beijing 100101, China*